












ARTICLE

Membrane budding is a major mechanism of in vivo platelet biogenesis

Kathryn S. Potts^{1,2*} , Alison Farley^{1,2*}, Caleb A. Dawson^{1,2*} , Joel Rimes^{1,2*} , Christine Biben^{1,2}, Carolyn de Graaf^{1,2} , Margaret A. Potts^{1,2} , Olivia J. Stonehouse^{1,2} , Amandine Carmagnac^{1,2}, Pradnya Gangatirkar^{1,2}, Emma C. Josefsson^{1,2} , Casey Anttila^{1,2} , Daniela Amann-Zalcenstein^{1,2} , Shalin Naik^{1,2}, Warren S. Alexander^{1,2}, Douglas J. Hilton^{1,2}, Edwin D. Hawkins^{1,2**} , and Samir Taoudi^{1,2**} 

How platelets are produced by megakaryocytes in vivo remains controversial despite more than a century of investigation. Megakaryocytes readily produce proplatelet structures in vitro; however, visualization of platelet release from proplatelets in vivo has remained elusive. We show that within the native prenatal and adult environments, the frequency and rate of proplatelet formation is incompatible with the physiological demands of platelet replacement. We resolve this inconsistency by performing in-depth analysis of plasma membrane budding, a cellular process that has previously been dismissed as a source of platelet production. Our studies demonstrate that membrane budding results in the sustained release of platelets directly into the peripheral circulation during both fetal and adult life without induction of cell death or proplatelet formation. In support of this model, we demonstrate that in mice deficient for NF-E2 (the thrombopoietic master regulator), the absence of membrane budding correlates with failure of in vivo platelet production. Accordingly, we propose that membrane budding, rather than proplatelet formation, supplies the majority of the platelet biomass.

Introduction

Since megakaryocytes (Mks) were identified by Wright (Wright, 1906; Wright, 1910) as the source of platelets (Plts), the cellular mechanism of Plt production has been a matter of sustained debate (Becker and De Bruyn, 1976; Behnke, 1969; French, 1967; Ihzumi et al., 1977; Italiano et al., 1999; Junt et al., 2007; Nishimura et al., 2015; Radley and Haller, 1982; Radley and Hartshorn, 1987; Zucker-Franklin and Petursson, 1984). When making his seminal discovery, Wright also observed long pseudopodial processes (known as proplatelets [proPlts]) that extended from Mks into the peripheral circulation, he speculated that these could be released into the blood flow to yield circulating Plts (Wright, 1906; Wright, 1910). Although it has been reported that Plts can be shed as a consequence of explosive cell death during inflammatory stress (Kowata et al., 2014; Nishimura et al., 2015; Yamada, 1957), the process of proPlt formation has been observed during both in vitro differentiation studies (Choi et al., 1995; Italiano et al., 1999) and intravital imaging experiments (Junt et al., 2007; Lefrançois et al., 2017; Zhang et al., 2012). Thus, proPlt formation has been broadly accepted as the universal Plt-forming mechanism. However, the

release of Plts from proPlts has not yet been directly observed in vivo; thus, the extent to which proPlts contribute to the Plt biomass remains unclear. Understanding the physiological Plt-forming process will resolve a fundamental biological question of historical standing and may help the field to overcome the in vitro scalability problem that limits cost-effective Plt production for clinical use (Ito et al., 2018; Nakamura et al., 2014; Thon et al., 2014).

We have developed quantitative 3D and 4D imaging methods that enable the behavior of Mks to be studied in their native environment at the scale of the whole organ. Thus, we could visualize Mks and Plt formation from the initiation of hematopoiesis in the early embryo, through fetal development, to adult life. From these studies, we found that while proPlt formation was a relatively rare phenomenon at all stages studied, robust Plt production was observed via plasma membrane budding. In support of the vital role of budding, we found that the severe thrombocytopenia observed in *Nfe2^{-/-}* mice was not associated with loss of in vivo proPlt formation, as had been proposed on the basis of in vitro assays (Lecine et al., 1998), but correlated with failure of membrane budding.

¹The Walter and Eliza Hall Institute of Medical Research, Melbourne, Australia; ²Department of Medical Biology, The University of Melbourne, Melbourne, Australia.

Correspondence to Samir Taoudi: taoudi@wehi.edu.au

*K.S. Potts, A. Farley, C.A. Dawson, and J. Rimes are co-first authors. **E.D. Hawkins and S. Taoudi are co-senior authors; K.S. Potts's present address is Department of Developmental and Molecular Biology, Albert Einstein College of Medicine, Bronx, NY.

© 2020 Potts et al. This article is distributed under the terms of an Attribution–Noncommercial–Share Alike–No Mirror Sites license for the first six months after the publication date (see <http://www.rupress.org/terms/>). After six months it is available under a Creative Commons License (Attribution–Noncommercial–Share Alike 4.0 International license, as described at <https://creativecommons.org/licenses/by-nc-sa/4.0/>).

Our findings indicate that the output of membrane budding can account for the maintenance of the steady-state circulating Plt mass through the consistent delivery of nascent Plts directly into the circulating blood. In addition, this occurs without signs of proPlt formation or cell death. Furthermore, in the adult bone marrow (ABM), we observed membrane budding in Mks that have previously been classified as sessile, suggesting that the role for these cells in Plt production have been significantly underestimated.

Results

Intravital imaging studies of Mks in the ABM have established the existence of proPlt formation and explosive fragmentation as mechanisms of Plt production (Junt et al., 2007; Nishimura et al., 2015); we sought to understand which mechanisms are used during prenatal life. Primitive (non-stem cell-derived) Mks appear in the yolk sac between embryonic day 8.5 (E8.5) and E10.5 (Potts et al., 2014, 2015; Tober et al., 2007) and in vitro are capable of generating classic proPlts composed of Plt-sized swellings interconnected by fine shafts (Fig. 1 A). Because these primitive Mks undergo rapid terminal differentiation in vitro and Plts rapidly expand in number from E9.5 to E10.5 (Potts et al., 2014; Tober et al., 2007), we reasoned that if proPlts were producing these Plts they would be abundant at these stages in vivo. 3D imaging of the intact yolk sac revealed that proPlt-like structures were rare ($2.9\% \pm 3.5\%$; Fig. 1, B and C); surprisingly, a high frequency ($35\% \pm 14\%$) of Mks with Plt-sized buds directly attached to the plasma membrane were observed in vivo (Fig. 1, B and C). In contrast, only proPlt formation was observed by primitive Mks when cultured in vitro (Fig. 1 D), suggesting that an alternative mechanism of Plt production might occur in vivo in the midgestation embryo.

We next investigated whether membrane budding also occurs from conventional (highly polyploid) Mks in the fetal liver (FL) and thus represents a more general prenatal Plt-forming mechanism. Using scanning electron microscopy, we observed relatively large cells with buds at the plasma membrane (Fig. 1 E). Transmission electron microscopy confirmed that buds were associated with polyploid Mks and that buds contained organelles (Fig. 1 F). Studying Plt formation using conventional 2D methods (such as transmission electron microscopy) limits the information that can be acquired for any given Mk. The FL is a soft tissue that can be easily dissected and optically cleared for 3D imaging, making it a tractable model for studying Mks in their natural environment. E13.5 FL were isolated and manually sliced into $\sim 500\text{-}\mu\text{m}$ sections to allow acquisition of full-volume images of intact Mks in situ at high magnification. This approach provided adequate spatial resolution for the detection of fine structures such as filipodia, proPlts, and membrane buds. Conversion of these large-volume images into high-content datasets through the creation of surface objects based on CD41 expression (identifying both Mks and Plts) allowed the extraction of multiple quantifiable parameters such as protein expression, DNA content, and cell size (Video 1). In combination with behavior classification, this approach allowed us to undertake the first unbiased in situ exploration of Mk behavior (Fig. 2 A and Fig.

S1). We found that (a) although Mks readily undergo proPlt formation in vitro (Fig. 2 Bi), proPlt-displaying Mks were rare in vivo ($1\% \pm 2\%$); however, $53\% \pm 8\%$ of Mks in the E13.5 FL displayed membrane buds (Fig. 2 Bii); (b) circulating Plts, free Plts in the FL, and Mk-associated buds exhibited similar size ranges (Fig. 2 C); (c) free Plts and buds contained the α -granule-associated proteins von Willebrand factor (VWF) and Plt factor 4 (Fig. 2 D); (d) buds exhibited Plt-like patterning of the key cytoskeletal proteins (Pertuy et al., 2014; Schwer et al., 2001; Thon et al., 2010, 2012) F-actin, myosin heavy chain 9, and β 1-tubulin (Fig. 2 E); and (e) the ploidy of budding Mks ranged from 2N to 16N, which was not significantly different from those that displayed no evidence of Plt production (Fig. 2, Fi and Fii). In contrast, the few instances of proPlt-forming Mks that were observed had a significantly lower ploidy range (2N–8N; Fig. 2 Fiii, $P < 0.05$ with Fisher's exact test and Bonferroni's correction). Thus, membrane bud formation was concurrent with Mk maturation (endoduplication).

To determine whether Plt buds are produced by the attached Mk in the FL, the lineage tracking *Confetti* system (Snippert et al., 2010) was used in combination with the Mk-specific *Pf4-Cre* mouse line (Tiedt et al., 2007). In the *Pf4-Cre:Confetti* system, Cre is continuously expressed in Mks, causing repeated inversion of the reporter cassettes which, depending on the ploidy of the Mk at time of activation, results in four resolvable *Confetti* configurations (Fig. 3 A and Fig. S2; see Materials and methods). To assess the developmental relationship between Mks and their associated buds, we scored their *Confetti* configurations. Of 732 buds associated with 184 Mks, 98% were configuration matches (Fig. 3, B and C). These data favor the model that membrane buds are derived from the attached Mk.

To determine whether the presence of membrane buds on Mks was caused by apoptosis, we stained whole-mount preparations of FL to detect the presence of active (cleaved) caspase-3, the effector of apoptotic cell death. Analysis of positive control samples treated with Camptothecin (a potent inducer of apoptosis) confirmed our ability to detect apoptosis if present, but we found that very few cells in the fresh liver were undergoing cell death (Fig. 3 Di). Quantification of active caspase-3 in the general Mk and Plt populations (Fig. 3 Dii) and within budding Mks (Fig. 3 Diii) revealed no evidence of apoptosis in situ. This is consistent with the observation that apoptosis must be restrained for effective Plt production (Josefsson et al., 2011).

To track the fate of membrane buds, we developed an ex vivo protocol that enabled 4D (3D + time) imaging of Mks within thick sections of FL. The principle of this in toto strategy is that to understand in situ Plt production, Mks must be preserved within an organotypic architecture. To this end, sections of FL were maintained in a serum-free medium widely used to induce proPlt formation (Norol et al., 1998), but without exogenous growth factor supplementation. This meant that any Plt-inducing factors were supplied by the FL explant. 3D images were acquired at 3–5-min time resolution for ≤ 24 h, and cellular behavior (Plt-forming mechanism and death) was manually annotated. After the generation of surface object tracks, we derived signature traces of changes in cell volume and sphericity that accompanied these behaviors.

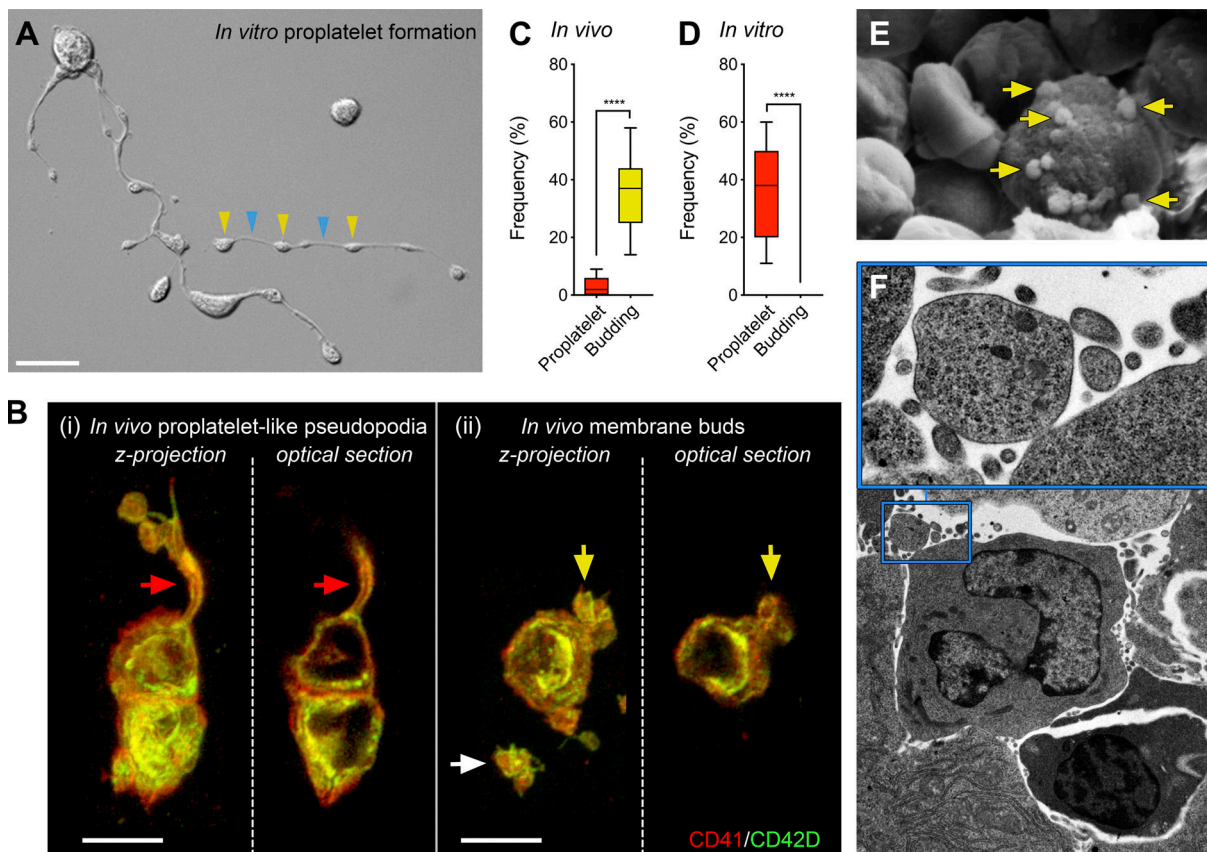


Figure 1. Identification of Plt-sized membrane buds. (A) Representative example of an in vitro proPlt from a E10.5 yolk sac Mk. Periodic swellings (yellow) interspersed by fine shafts (blue); $n = 15$ independent experiments. Scale bar, 20 μm . (B) Confocal 3D z-projections and optical sections from whole-mount yolk sac showing proPlt-like extensions (i, red arrows) and membrane buds (ii, yellow arrows). White arrow, free Plt; $n = 15$ independent experiments. Scale bars, 10 μm . (C) In vivo frequency of Plt-forming morphologies of Mks in the E10.5 yolk sac; $n = 7$ independent mice. $P < 0.0001$, unpaired two-tailed t test. (D) In vitro frequency of Plt-forming morphologies of E10.5 Mks after 3 d of culture ($n = 15$ independent experiments). $P < 0.000001$, unpaired two-tailed t test. (E and F) Membrane buds (arrows) associated with polyploid cells in E13.5 FL observed using scanning (E) and transmission (F) EM; $n = 3$ independent experiments.

Of the 122 Mks analyzed: 57% did not engage in Plt formation or undergo death, these cells maintained stable cell volume and sphericity (Fig. 4 Ai); 2% underwent a pyroptosis-like cell death (Lamkanfi and Dixit, 2010), during which cellular volume rapidly expanded before an acute collapse and cessation of movement (Fig. 4 Aii); 3% underwent proPlt formation, initiation of which resulted in a concomitant increase in volume and decrease in sphericity as proPlts were extended (Fig. 4 Aiii and Video 2); and direct release of Plts via plasma membrane budding was observed in 38% of Mks, not accompanied by marked change in volume or sphericity (Fig. 4, Aiv and B; and Video 3). Importantly, none of the 143 observed budding events gave rise to proPlts. The volume of nascent Plts derived from budding was similar to that of free Plts (Fig. 4 C), and we noted that Plt release occurred through the liberation of single or multiple Plts in a single shedding event (Fig. 4 D). Each Mk was tracked for 1–15 h (7 h median), and the time observed after the release of the first bud was 1–15 h (4 h median). No budding Mks were observed to undergo cell death (the censoring event being the end of experiment or exit from the field of view), which is consistent with the absence of apoptosis in budding Mks in vivo (Fig. 3 D). As is the case in the ABM (Zhang et al., 2012), FL Mks were in direct

association with the vasculature, and VWF-loaded buds were frequently observed protruding through the endothelial lining (Fig. 4 E and Video 4), thereby providing opportunity to deliver Plts directly into the peripheral circulation.

To test whether Plt production via membrane budding is restricted to the prenatal organism, we studied Mks in the ABM using previously described two-photon intravital imaging of the calvarium (Duarte et al., 2018; Hawkins et al., 2016). The behavior of hematopoietic cells in calvarial bone marrow (BM) accurately reflects that of other long bones (Koechlein et al., 2016; Reismann et al., 2017) but has the advantage that the surrounding bone is thin enough to allow visualization of the marrow without the need to manipulate the bone (Hawkins et al., 2016), permitting 4D imaging of the entire marrow. We found that large Mks were highly abundant within the BM (Fig. 5 A), and of 442 Mks observed in 3D z-projections, 1% (4 of 442) had associated proPlts, with the remaining Mks appearing sessile, with either a classic circular or complex morphology (Fig. 5, B and C).

The scope of past Mk intravital imaging experiments has been constrained by the necessity to select regions of interest, imposing restrictions on either the number of cells that can be

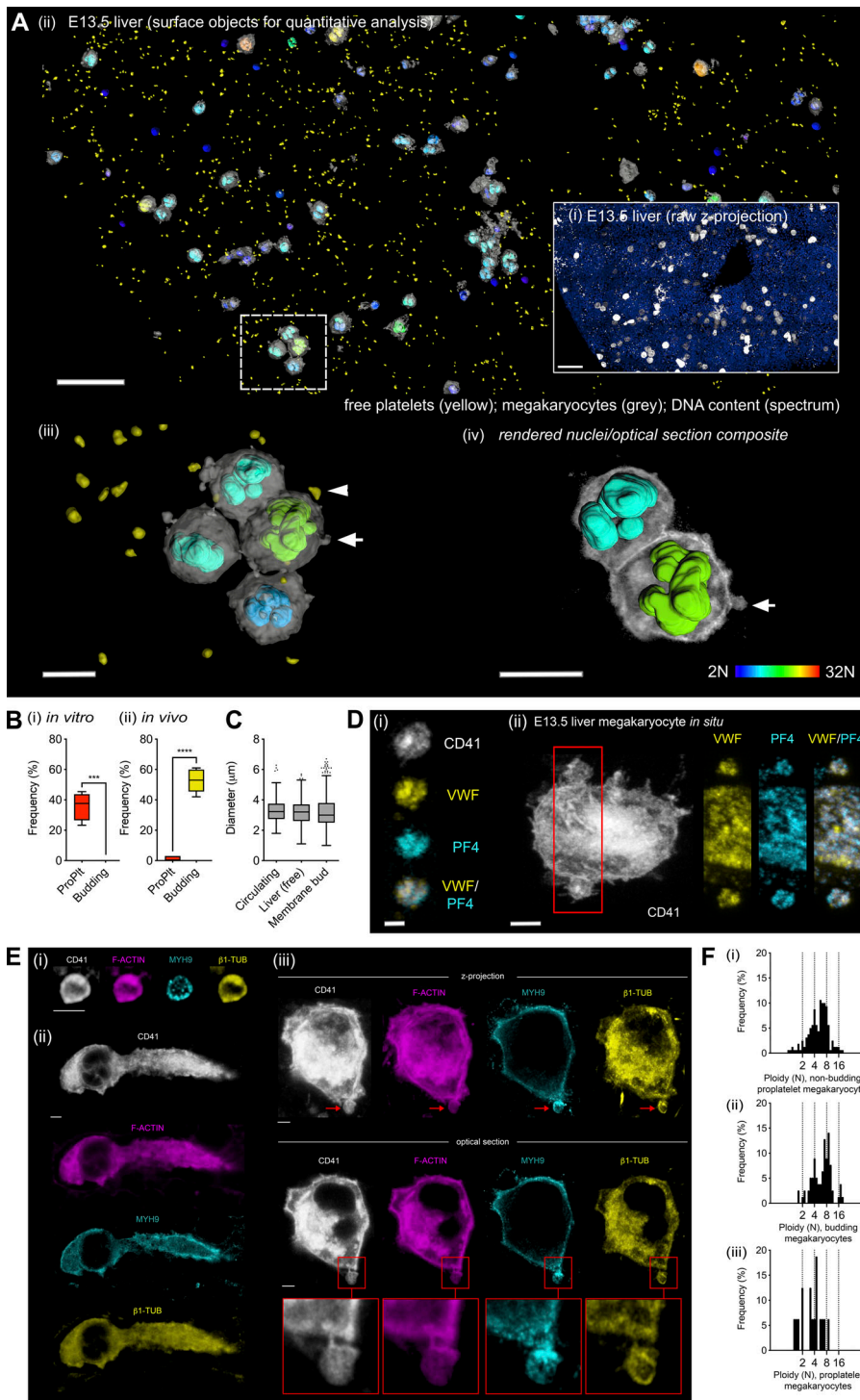


Figure 2. Quantitative analyses of Mks in situ. **(Ai)** High-volume 3D confocal image of E13.5 FL section showing Mks and Plts (anti-CD41, gray), and nuclei (DAPI, blue). Scale bar, 100 μm . **(Aii)** Surface objects rendered from raw data: Mks (gray); free Plts (yellow); nuclei pseudocolored according to DNA content (DAPI, color spectrum). Scale bar, 100 μm ; $n = 5$ independent experiments. **(Aiii)** Enlargement of box: Mk with attached bud (arrow); free Plt (arrow-head). Scale bar, 20 μm . **(Aiv)** Optical section from raw data of budding Mk in iii; nuclear surface objects overlaid. Scale bar, 20 μm . **(B)** Quantitation of *in vitro* (i) and *in vivo* (ii) Plt-forming mechanisms ($n = 4$ –5 independent experiments). $P = 0.0002$ (i) and $P < 0.0001$ (ii), unpaired two-tailed *t* test. **(C)** Diameters of circulating Plts ($\sigma = 236$), free Plt in the FL ($\sigma = 406$), and Mk-associated buds ($\sigma = 749$; $n = 3$ independent experiments). $P = 0.32$, one-way ANOVA. **(Di)** Representative image of Plt-associated proteins in free Plt in E13.5 FL. Scale bar, 2 μm . **(Dii)** Representative image of Plt-associated proteins in E13.5 FL. Scale bar, 2 μm . **(Ei)** Representative example (optical sections) of F-actin, MYH9, and β 1-TUBULIN (β 1-TUB) staining observed in free Plts in E13.5 FL. **(Eii)** Representative example of an optical section of a proPlt-forming Mk in E13.5 FL. **(Eiii)** Representative example of an optical section from a budding Mks in E13.5 FL showing the presence of a Plt-like pattern of MYH9 and β 1-TUB staining in the membrane buds. Optical sections are taken from the boxed regions. Scale bars, 3 μm . $n = 6$ independent experiments. **(F)** In situ ploidy values for nonbudding Mks (i, $\sigma = 160$), budding Mks (ii, $\sigma = 78$), and proPlt-forming Mks (iii, $\sigma = 16$); $n = 5$ independent experiments.

observed or the duration of observation. We circumvented this problem by collecting 3D tiled images of the entire calvarial BM at sub-4-min intervals for 6 h. Using this approach, we were able to undertake unbiased tracking of the steady-state behavior of all Mks resident in the BM in parallel (Video 5). Of the 825 Mks observed, only 2% (18 of 825) underwent proPlt formation (Fig. 5 D). We observed that proPlt formation took 18–336 min (mean 103 min) to complete, measured from the time of initiation to detachment (Fig. 5, E and F; and Video 6). 7% (58/825) of

Mks generated thick extensions that did not develop into proPlts (Video 7), and 91% of Mks appeared to be sessile (no observed proPlt formation or development of thick extensions; Fig. 5 D).

ProPlt-forming Mks in the BM underwent marked decreases in volume through the period of observation (Fig. 5 G). If proPlt formation was the major driver of *in vivo* Plt biogenesis, it is expected that over a 6-h period the vast majority of Mks would have undergone proPlt formation (Junt et al., 2007) and so would have exhausted their cytoplasmic volume. Contrary to

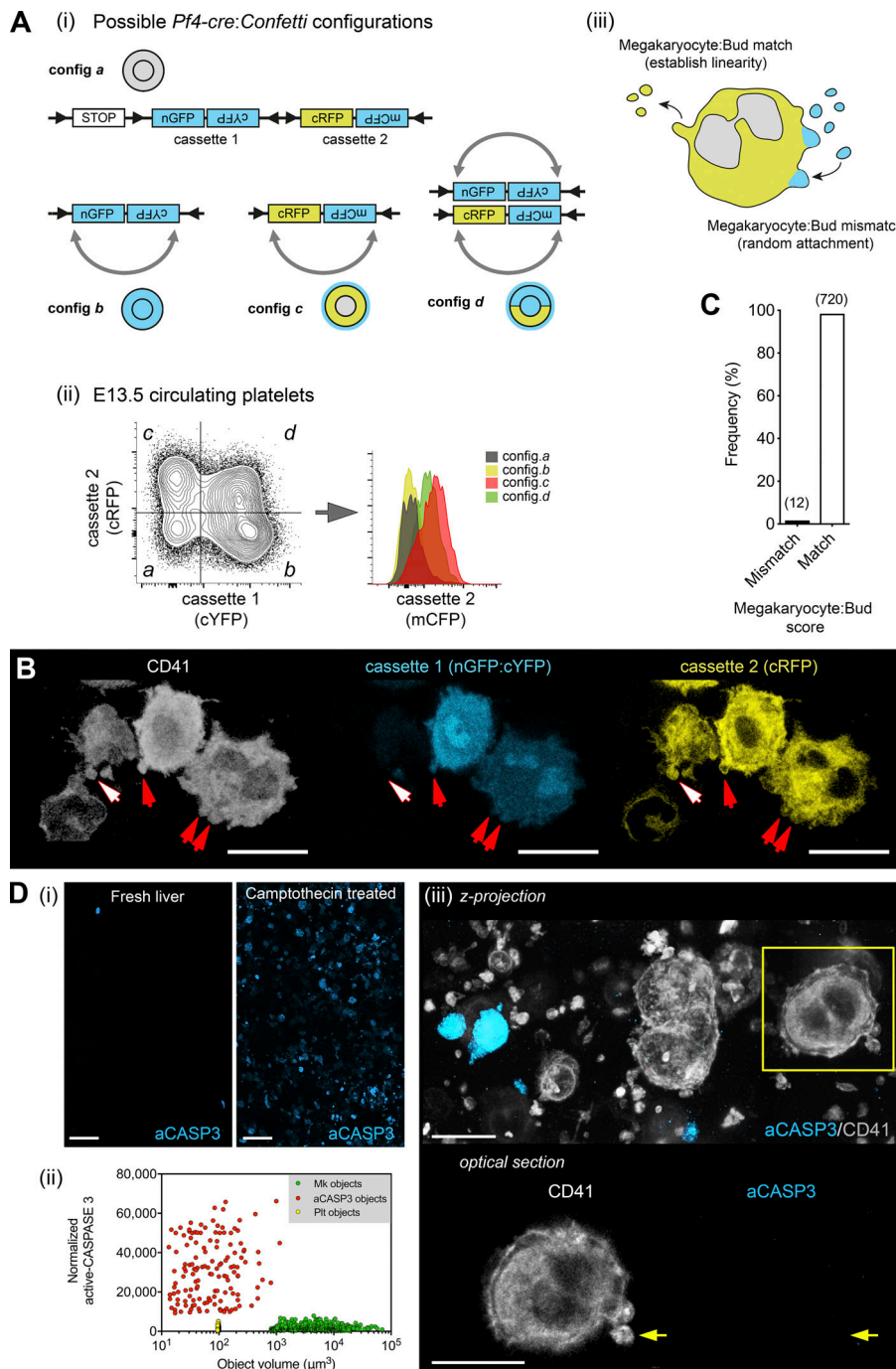


Figure 3. Buds derive from the attached Mk. (Ai) Possible *Pf4-Cre:Confetti* cassette configurations after Cre-mediated recombination. (Aii) Flow cytometric analysis of E13.5 circulating Plts; note that mCFP is expressed only in configurations c and d Plts (histogram). (Aiii) Mk:bud match interpretation. (B) Optical section through configuration c (white arrow) and d (red arrow) budding Mks in E13.5 FL. Scale bar, 10 μ m. (C) Mk:bud configuration scores ($n = 732$ buds, 184 Mks, $n = 5$ independent experiments). (Di) Representative example of a 3D z-projection of active CASPASE-3 (aCASP3) detection in fresh E13.5 FL (anti-aCASP3, blue; anti-CD41, gray). Cells undergoing apoptosis (aCASP3⁺) were rare. FL slices incubated with 4 μ M Camptothecin (a potent inducer of apoptosis) were used as positive controls ($n = 4$ independent experiments). Scale bars, 50 μ m. (Dii) Volume-normalized aCASP3 content of Plts and Mks compared with CD41⁻ aCASP3⁺ objects ($n = 2,100$ Plts, 1,430 Mks, 139 CD41⁻ aCASP3⁺ objects; $n = 4$ independent experiments). (Diii) Representative example of aCASP3 detection in situ, confirming the absence of CASPASE-3 activation in budding Mks. Optical section of budding Mk (boxed region); yellow arrow indicates a membrane-associated bud. Scale bars, 20 μ m.

this prediction, the volume of non-proPlt-forming/sessile Mks remained relatively stable (Fig. 5 H). Based on deductive reasoning, it has been estimated that each Mk is capable of producing a total of 100–4,000 Plts; thus, the Mk population is thought to provide the organism with tens of millions of new Plts per hour (Fuentes et al., 2010; Kaufman et al., 1965; Lefrançois et al., 2017). Given the hourly rate of Plt formation, these data indicate that in vivo Plt production does not result in acute Mk exhaustion.

We reasoned that because instances of proPlt formation were rare (Fig. 5, C and D) and took >1 h for proPlt detachment to occur (Fig. 5, E and F), this process was unlikely to be sufficient

to maintain steady-state Plt numbers. Given our observations in the prenatal organism, we hypothesized that if membrane budding is a conserved feature of Mk biology, then Mks previously classified as sessile could be candidates for suppliers of Plt production.

Unlike the FL explant system, capturing potential budding events in live adults is complicated by the high velocity of the circulating peripheral blood. To account for this, we adopted a focused high-time-resolution approach, for which 45 sessile Mks (which included both circular Mks and those with complex morphology) were imaged in 3D (15–30- μ m range in z-axis) at a 2–3-s time resolution for 10–15 min. To distinguish Mk-associated buds from passing Plts, we applied the criteria

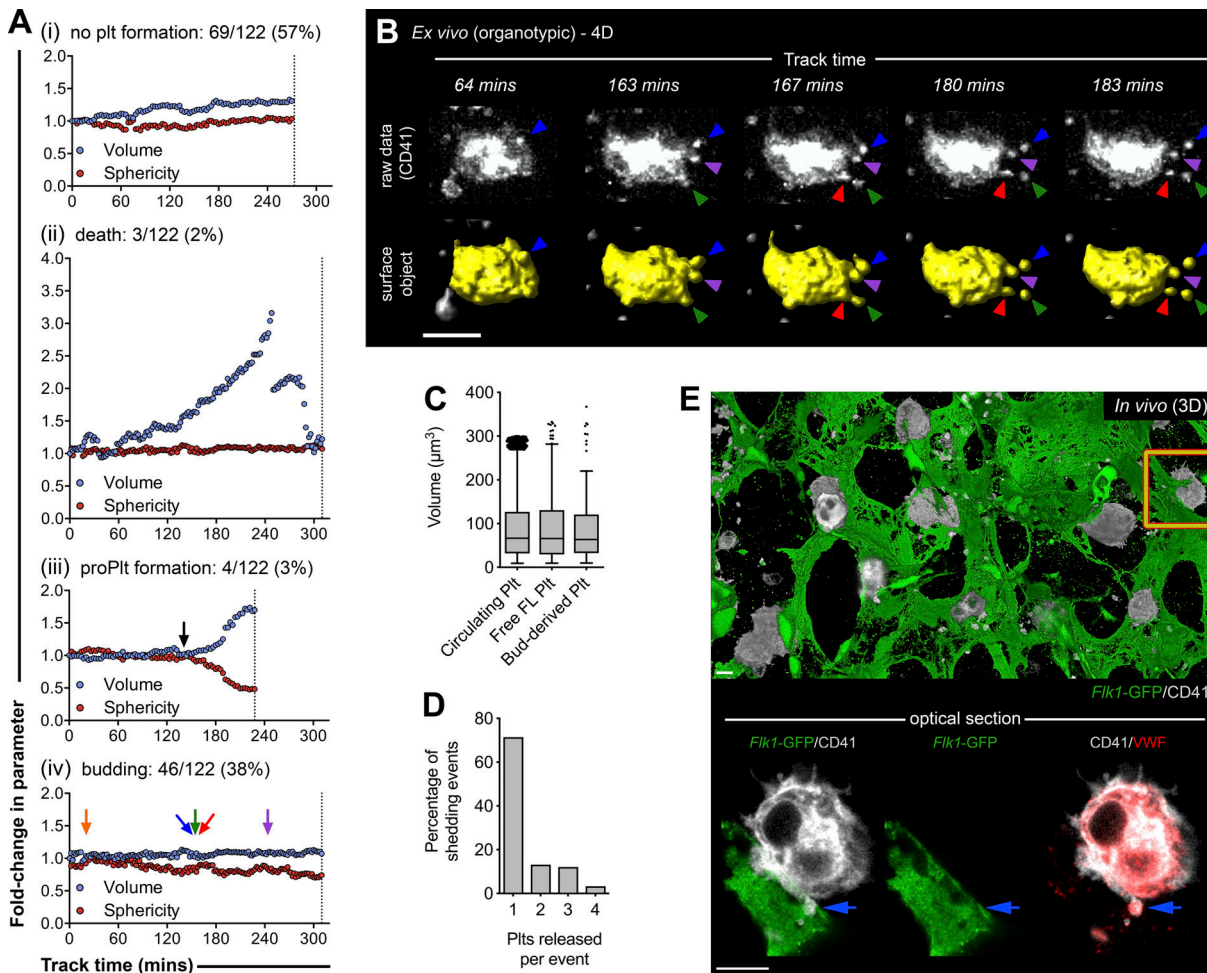


Figure 4. Buds are directly released as Plts. (A) Mk behavior tracks from E13.5 FL organotypic cultures. Representative examples of changes in cell volume and sphericity of Mks that did not undergo Plt production (i); died (ii); formed proPlts (iii); and released Plts via budding (iv). Black arrow (iii), initiation of proPlt formation; colored arrows (iv) highlight Plt release events. The absolute count and frequency of each Mk behavior is indicated. Vertical line indicates end of track. **(B)** Stills from a budding Mk movie (see Video 3). Colored arrows highlight Plt release events. Scale bar, 10 μ m. **(C)** Volume of circulating Plts, free FL Plts ($n = 738$) present at the start of experiment, and nascent Plts ($n = 138$) released by budding. $P = 0.95$, one-way ANOVA. **(D)** Number of Plts released per shedding event. **(E)** 3D z-projection of E13.5 FL Mks (CD41, gray) and endothelium (*Flk1*-GFP, green) in vivo. Optical section from boxed region. Distribution of Plt-associated protein VWF indicated in red. Scale bars, 10 μ m. $n = 4$ independent experiments. Blue arrow, trans-endothelial bud.

developed from our FL studies: classification as a bud required continuity between the Mk and the attached object. If this condition was not met, the object was classified as a passing Plt (Fig. S3). Of the 45 sessile Mks investigated, a strikingly high proportion (84%) were observed releasing Plts via membrane budding directly into the circulating blood without the formation of a proPlt intermediary (Fig. 5, I and J; and Video 8). Importantly, none of the budding events observed resulted in proPlt formation. Plt production via budding occurred at a rate of 2 Plts/min (Fig. 5, K and L), which extrapolates to a production rate of 120 Plts per Mk/hr. Consistent with membrane buds being poised for release as nascent Plts, the size of buds was similar to that of Plts in the peripheral circulation (Fig. 5 M).

Next, we assessed to what extent Mk budding in the calvarial BM is representative of that in other Mk-containing sites. We performed extensive investigations of Mk distribution and morphology in all major sources of BM (pelvis, long bones, ribs and sternum, skull, and spine). Mks were similarly frequent in

all sources of BM (Fig. 6 A). Not only was the frequency of Mks higher in the BM compared with spleen and lungs (Fig. 6 B), but by quantifying Mk numbers in the majority of bones within the skeleton, we found that the BM harbored the vast majority of all the Mks in the adult: 79% in the BM, 13% in the spleen, and 8% in the lungs (Fig. 6 C and Fig. S4). To generate a broad snapshot of Plt-forming morphologies, Mks were scored in thick sections of the femur, pelvis, spleen, and lung (Fig. 6 D and not depicted). This revealed that at any given time ~1% of Mks were undergoing proPlt formation but ~50% were budding (Fig. 6, E-G). Consistent with our intravital imaging data (Fig. 5 M), membrane buds in the BM were similar in size to circulating Plts (Fig. 6 H). The exception to this trend was the lungs, which contained fewer Mks (Fig. 6 C), but a large proportion were undergoing proPlt formation (Fig. 6 I). This appeared to occur mostly from Mks located within the lung vasculature. We noted that membrane buds in the BM and spleen contained F-actin structures that were continuous with the F-actin present in

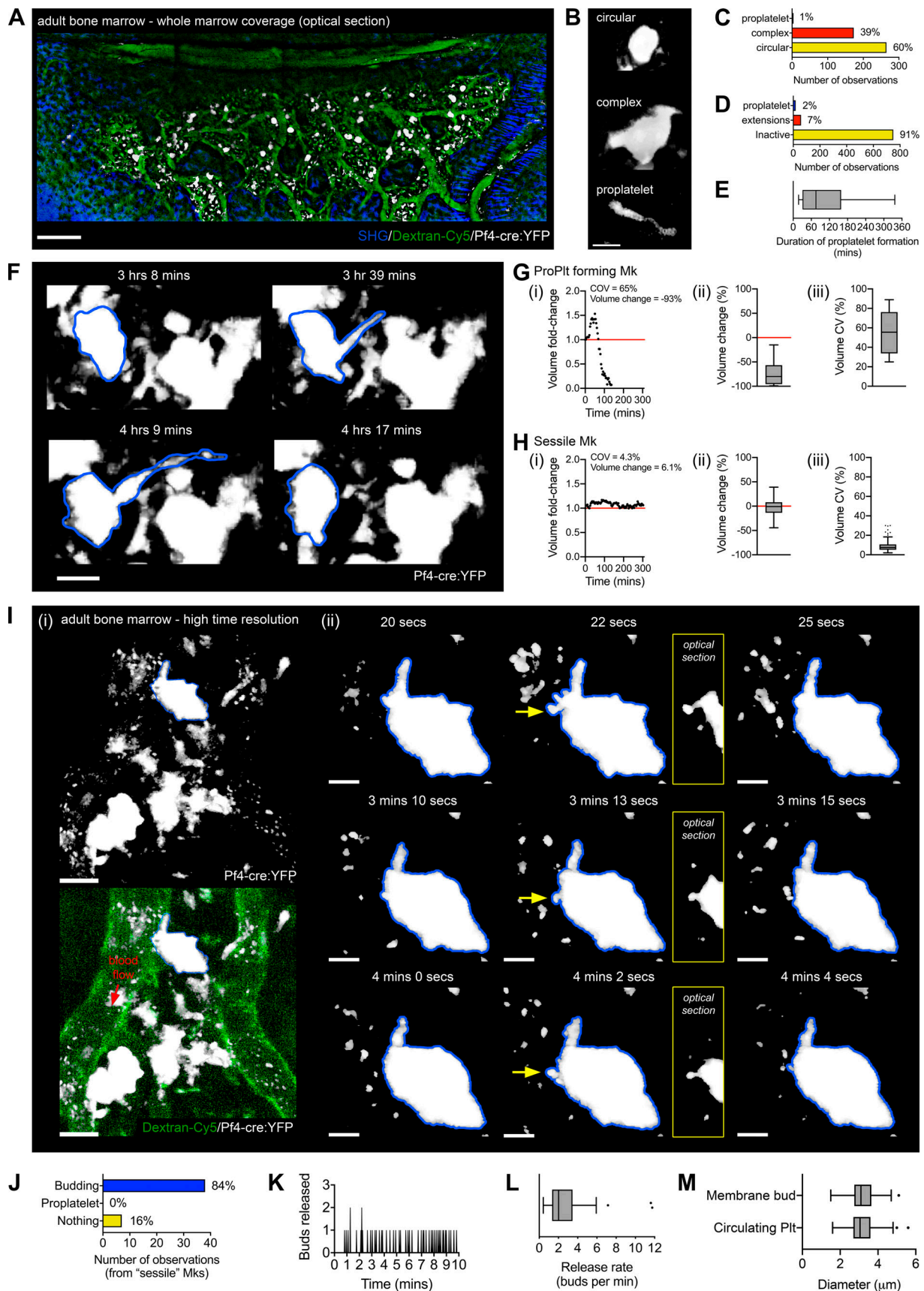


Figure 5. **Mk budding in the ABM.** (A) Optical section from a 3D z-projection of the adult calvarial BM showing Mks (*Pf4-Cre:YFP*, gray), bone (SHG signal, blue), and vasculature (Dextran-Cy5, green). Scale bar, 200 μ m. (B) Representative examples of observed BM Mk morphologies. Scale bar, 20 μ m.

(C) Frequency of observed Mk morphologies within the BM. Cumulative of three experiments. **(D)** Frequency of observed BM Mk behaviors during 4D intravital imaging over 6 h. Cumulative: $\sigma = 825$; $n = 2$ independent experiments. **(E)** Duration of proPlt formation observed from individual Mks in 4D intravital imaging. Cumulative: $\sigma = 18$; $n = 2$ independent experiments. **(F)** 4D intravital time series of a proPlt-forming Mk (blue outline). Scale bar, 20 μm . **(G)** Representative example of in situ volume fold-change of a proPlt-forming Mk (i), summary of volume change (ii), and summary of volume coefficient of variation (CV) of in situ proPlt-forming Mks ($\sigma = 10$ Mks, $n = 2$ independent experiments; iii). **(H)** Representative example of in situ volume fold-change of a sessile Mk (i), summary of volume change (ii), and summary of volume CV of in situ sessile Mks ($\sigma = 183$ Mks, $n = 2$ independent experiments; iii). **(I)** Overview z-projection of sessile calvarial Mks (YFP, gray) associated with the vasculature (visualized using Dextran-Cy5, green). Mk of interest outlined in blue. The direction of the flow of blood is indicated by a red arrow. **(II)** 4D intravital time series (2-s resolution) of a sessile Mk (outlined in blue) releasing a Plts into the peripheral circulation via plasma membrane budding. Yellow arrow indicates location of bud formation. Attachment of the bud before presumptive release was confirmed using optical sections (inset yellow boxes). Scale bar, 10 μm . **(J)** Observed BM Mk behaviors during high-time-resolution (2-s) intravital imaging. Cumulative, $\sigma = 45$ Mks; $n = 4$ independent experiments. **(K)** Example of the frequency of Plt release events from an individual Mk in vivo. **(L)** Observed in vivo Plt release/budding rate from individual Mks ($\sigma = 37$ Mks). Cumulative, $n = 4$ independent experiments. **(M)** Comparison of observed membrane bud ($\sigma = 129$) and circulating Plt ($\sigma = 264$) diameters. Cumulative, $n = 4$ independent experiments. $P = 0.61$, two-tailed unpaired t test.

the peripheral zone of the attached Mk (Fig. 6, J–L), suggesting the involvement of the cytoskeletal cortex in Plt formation and/or release. In contrast, discrete F-actin structures were absent in Mks undergoing proPlt formation in the lungs (Fig. 6 M).

Disassembly of peripheral zone microtubules occurs as proPlt-forming BM Mks enter the lumen of the vasculature (Brown et al., 2018). This process is morphologically reminiscent of uropod elongation that has been observed to accompany the migration of multiple hematopoietic lineages both in vivo and in vitro (Hyun et al., 2012; Renkawitz et al., 2019). Leveraging our long-term intravital imaging data of the calvarial BM, the outcome of in vivo proPlt formation was explored. We observed that 20% of proPlt-forming Mks released large fragments into the circulation, and 60% appeared to either exhaust their cytoplasm or fully enter into the peripheral circulation without proPlt release (Fig. 7 A). To resolve these possibilities, we imaged Mks at 15 frames/s and found clear evidence that polyploid Mks could exit from the BM space during proPlt formation (Fig. 7 B and Video 9).

The sum of evidence indicates that membrane budding accounts for a major proportion of the Plt biomass during prenatal and adult life. Furthermore, these data suggest that proPlt formation and membrane budding are likely to be mechanistically distinct processes. To test this, we investigated how budding and proPlt formation were affected in *Nfe2l3*^{-/-} mice. NF-E2 (nuclear factor, erythroid 2) is a critical transcriptional regulator of in vivo Plt production (Levin et al., 1999; Shivdasani et al., 1995); in the absence of NF-E2, Mks are present in normal numbers in embryonic and adult mice, but they lack circulating Plts (Lecine et al., 1998; Potts et al., 2015; Shivdasani et al., 1995). Because FL-derived *Nfe2l3*^{-/-} Mks do not generate proPlts in vitro (Lecine et al., 1998), it has been suggested that thrombocytopenia in *Nfe2l3*^{-/-} mice is likely caused by failure of proPlt formation in vivo. Given that our findings brought into question the contribution of proPlt formation to the maintenance of Plt biomass, we investigated the in vivo Plt-forming processes affected in thrombocytopenic *Nfe2l3*^{-/-} mice.

At E14.5, *Nfe2l3*^{-/-} circulating Plts were 1% of *Nfe2l3*^{+/+} numbers (Fig. 8 Ai). At preceding developmental stages in the yolk sac (Fig. 8 Aii) and the FL (Fig. 8, Aiii–D), the frequency of Mks undergoing proPlt formation was not significantly different between *Nfe2l3*^{+/+} and *Nfe2l3*^{-/-} samples; however, membrane budding was reduced to 7 and 17% of wild-type numbers, respectively. These data are consistent with membrane budding being a major contributor to the Plt biomass.

Nfe2l3^{-/-} mice die in early neonatal life (Shivdasani et al., 1995), but *Nfe2l3*^{-/-} Mks are produced in the adult after transplantation of FL cells (Lecine et al., 1998). To investigate whether defective thrombopoiesis in the *Nfe2l3*^{-/-} adult hematopoietic system was associated with failure of Mk membrane budding, we generated adult hematopoietic chimeric mice. *Nfe2l3*^{+/+} or *Nfe2l3*^{-/-} E13.5 FL (GFP⁻) were transplanted into lethally irradiated mice that ubiquitously expressed GFP. After 4–5 wk, peripheral blood was taken to measure hematopoietic chimerism in circulating Plts and RBCs; BM, spleen, and lungs were harvested for large-scale confocal analysis to assess the Plt-forming morphologies of donor cell-derived (GFP⁻) Mks (Fig. 9 A). In recipient mice transplanted with *Nfe2l3*^{+/+} cells, donor-derived reconstitution accounted for the vast majority of the circulating Plt and RBC pools (Fig. 9 Bi). In contrast, although *Nfe2l3*^{-/-} recipient cells successfully reconstituted RBCs, they exhibited significantly reduced reconstitution of the Plt compartment. The vast majority of RBCs, however, were derived from *Nfe2l3*^{-/-} donor cells: only the recipients' own GFP⁺ cells had contributed to Plts (Fig. 9, Bii). Thus, as expected, Plt production from *Nfe2l3*^{-/-} Mks was dramatically impaired. Assessment of donor-derived Mks in the BM and spleen revealed a modest increase in proPlt formation by *Nfe2l3*^{-/-} cells, but the frequency of Mks with membrane buds was significantly reduced (Fig. 9, Ci, Cii, D, and E). ProPlt formation in the lungs was not significantly different between *Nfe2l3*^{+/+} and *Nfe2l3*^{-/-}, but membrane budding was almost absent (Fig. 9, Ciii and F). Of note, free proPlts and proPlt fragments were observed in both E13.5 *Nfe2l3*^{+/+} and *Nfe2l3*^{-/-} fetuses and in adult mice reconstituted with both *Nfe2l3*^{+/+} and *Nfe2l3*^{-/-} cells (Fig. 9, G and H). These data indicate that in both the fetus and the adult, the predominant effect of *Nfe2l3* deletion in vivo is a severe reduction in membrane budding.

Transcriptome-wide changes in culture-derived FL *Nfe2l3*^{-/-} Mks have been previously described (Chen et al., 2007; Fujita et al., 2013; Motohashi et al., 2010; Takayama et al., 2010); however, there are currently no investigations of changes that occur in *Nfe2l3*^{-/-} primary Mks in vivo. Because proPlt formation is favored over membrane budding in vitro, we performed single-cell RNA-sequencing (scRNA-seq) on primary in vivo *Nfe2l3*^{+/+} and *Nfe2l3*^{-/-} Mks from E13.5 FLs and donor-derived (GFP⁻) ABM Mks from adult hematopoietic chimeras to understand the broad molecular changes that underpin the loss of membrane budding. Sequencing metrics, quality control, and downstream analysis are described in Table S2 and Fig. S5. Mks

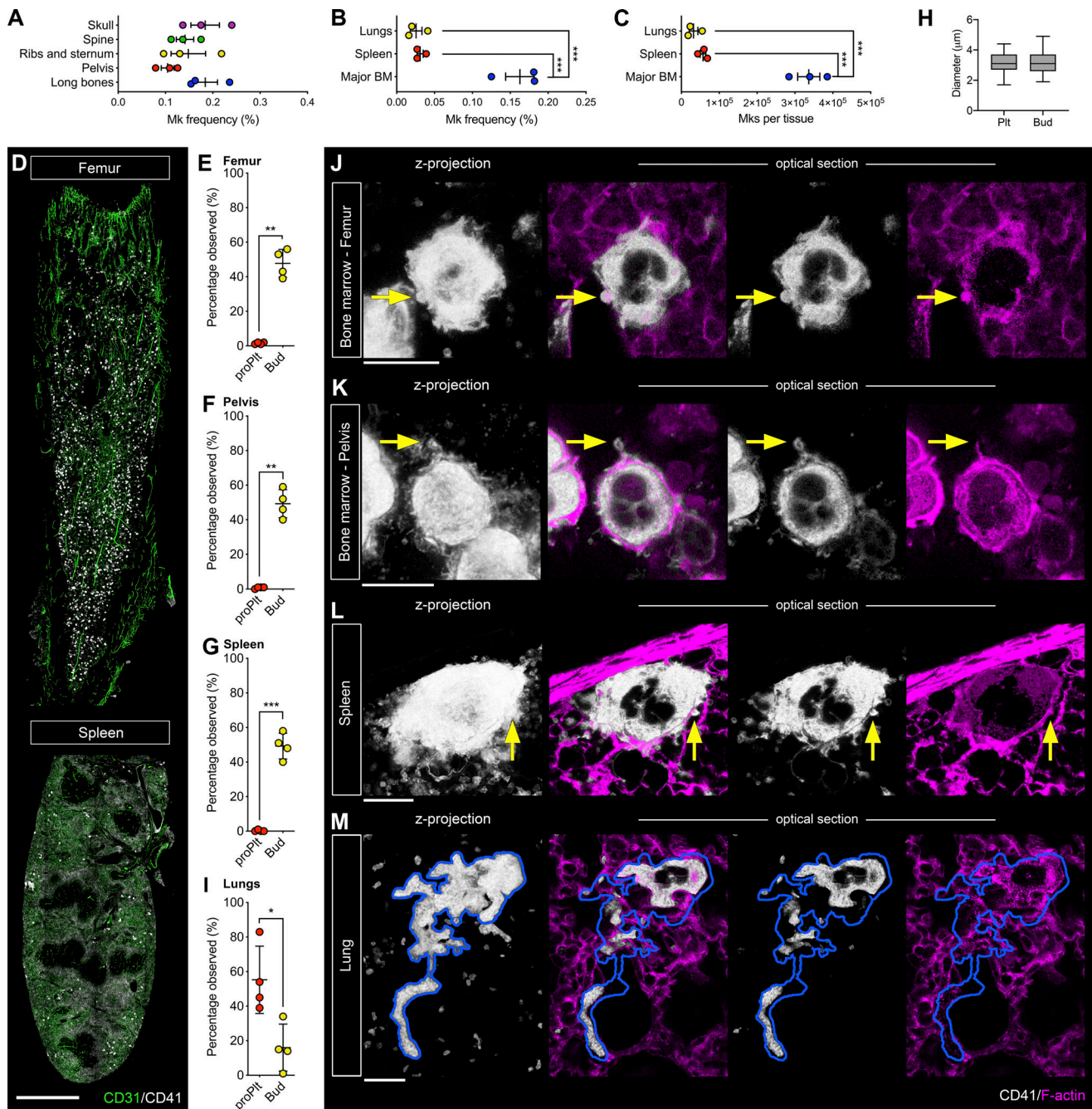


Figure 6. Mk budding occurs in multiple locations. (A–C) Frequency of Mks in major BM sites as quantified by flow cytometry (A), $P = 0.25$ one-way ANOVA; comparison of Mk frequency in the combined BM, spleen, and lungs (B), $***, P < 0.0006$, one-way ANOVA with Tukey’s multiple comparisons test; and distribution of absolute Mk numbers in the BM, spleen, and lungs (C), $***, P < 0.0001$; $****, P < 0.0001$, one-way ANOVA with Tukey’s multiple comparisons test. Data derived from three independent mice. **(D)** Representative examples of large-scale z-projections showing the structure of vasculature (CD31, green) and Mk (CD41, gray) distribution in the femoral BM and spleen ($n = 4$ independent experiments). Scale bars, 1,000 μm . **(E–G)** Frequency of observed Mk morphologies within the femoral BM ($\sigma = 1,435$; $n = 4$ independent mice), $P = 0.0014$, two-tailed unpaired t test with Welch’s correction (E), pelvic BM ($\sigma = 314$; $n = 4$), $P = 0.0012$, two-tailed unpaired t test with Welch’s correction (F); and spleen ($\sigma = 458$; $n = 4$), $P = 0.0009$, two-tailed unpaired t test with Welch’s correction (G). **(H)** Comparison of membrane bud ($\sigma = 176$) and free Plt ($\sigma = 312$) diameters in the femoral BM; $P = 0.94$, two-tailed unpaired t test with Welch’s correction. Cumulative, $n = 4$ independent experiments. **(I)** Frequency of observed Mk morphologies within the lungs ($\sigma = 75$; $n = 4$), $P = 0.019$, two-tailed unpaired t test with Welch’s correction. Cumulative, $n = 4$ independent experiments. **(J–M)** Representative examples of F-actin distribution in budding Mks in the femur (J), pelvis (K), and spleen (L), and a proPlt-forming Mk in the lungs (M). Scale bars, 20 μm . For I–L, CD41 is shown in gray and F-actin in magenta. Membrane buds indicated with yellow arrow; proPlt-forming Mk outlined in blue.

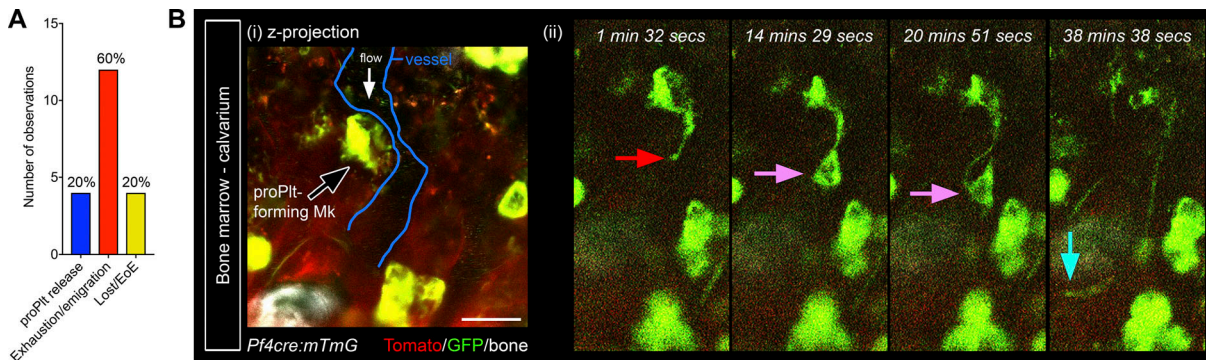


Figure 7. ProPlt formation can precede exit of Mks from the BM. (A) Cumulative scores of observed outcomes of proPlt-forming BM Mks, derived from low-time-resolution 4D data over 4–5 h ($\sigma = 20$; $n = 3$). **(B)** Example of a 3D intravital time series captured at 15 frames/s at a single z-position, showing the emigration of a polyplod Mk during proPlt formation. **(Bi)** 3D z-projection highlighting an Mk of interest (black arrow) before time-lapse imaging. **(Bii)** Snapshots from time series. Red arrow, leading edge of primary proPlt extension; pink arrows, nucleated region of proPlt-forming Mk leaving the BM space (nuclei as distinguished by the regional absence of membrane-bound GFP); cyan arrow, secondary proPlt extension formed after the disappearance of the nucleus. *Pf4cre:mTmG* non-Mk (red) and Mk (green); second harmonic signal generation, bone (gray). Scale bar, 50 μ m.

were identified with lineage signatures generated from Haemopedia mouse RNA-seq (Fig. S5; Choi et al., 2019).

The number of genes that were differentially expressed (DE) in *Nfe2^{-/-}* Mks varied according to developmental stage: in E13.5 *Nfe2^{-/-}* Mks, 337 genes were DE (157 genes down-regulated and 180 up-regulated); in ABM *Nfe2^{-/-}* Mks, 1,046 genes were DE (623 genes down-regulated and 423 up-regulated; Fig. 10 A, Data S1, and Data S2). To identify genes likely to be involved in membrane budding in both the fetus and the adult, we investigated those genes that were commonly DE in both E13.5 FL and ABM *Nfe2^{-/-}* Mks: 36 genes were commonly down-regulated and 79 were commonly up-regulated (Fig. 10, B and C, and Table S3 and Table S4). We performed a gene set test on genes previously identified as bound by NF-E2 and DE in *Nfe2^{-/-}* versus *Nfe2^{+/+}* E13.5-derived in vitro-cultured Mks (Fujita et al., 2013). These gene sets were significantly DE in primary E13.5 FL *Nfe2^{-/-}* Mks (false discovery rate $<10^{-7}$), but not in the adult MKs (Fig. 10, Aii and B). Thus, the broad transcriptional changes that occur in *Nfe2^{-/-}* are largely dependent on developmental stage.

Of genes that were commonly down-regulated, four (*Tuba4a*, *Rgs18*, *Mef2c*, and *Cdc20*) have previously been shown to be important for normal Plt production (Delesque-Touchard et al., 2014; Gekas et al., 2009; Strassel et al., 2019; Trakala et al., 2015). Gene ontology (GO) term enrichment analysis of commonly DE genes indicated that failure of membrane budding was accompanied by the up-regulation of genes associated with catabolic and metabolic processes (Fig. 10 Ci) and the down-regulation of genes associated with cell cycle transition, Mk differentiation, and cytoskeletal organization (Fig. 10 Cii and Table S5).

Our findings suggest that membrane budding is a major driver of in vivo Plt production and is conserved in both fetal and adult Mks. Furthermore, we show that in vivo proPlt formation and membrane budding are mechanistically distinct processes.

Discussion

It has previously been problematic to reconcile the high rate of adult Plt production with the observation that the vast majority of Mks appeared inactive (Lefrançois et al., 2017). Implementation

of an unbiased quantitative strategy to combine extensive organ-wide intravital analysis with rapid-time-resolution visualization of in situ Mk behavior has allowed us to propose a solution: rather than being sessile, a high frequency of Mks in multiple BM sites and the spleen are actively engaged in Plt production via membrane budding. In contrast to the temporally extended process of proPlt formation, budding is rapidly executed to deliver a consistent supply of Plts. Our findings provide a robust dataset to determine Plt production from Mks in vivo, based on the direct visualization of Plt production as opposed to quantitative deduction alone.

By considering the total number of Mks in the major ABM spaces and applying our experimentally observed frequency and rate of Plt production in the calvarial BM, we calculate that Plt budding from BM Mks alone could produce $\sim 3.4 \times 10^7$ Plts/hr, which accounts for 89% of the estimated 3.82×10^7 Plts/hr required to maintain stable circulating numbers (see Materials and methods). Because the in vivo Mk lifespan is unknown, the total number of Plts each individual Mk can produce in vivo remains unknown. We found that although only a small fraction of Mks in the adult are located in the lungs, the majority of these cells were undergoing proPlt formation. It therefore remains possible that Plt production via proPlt formation occurs in the lungs rather than the BM. However, because of the relatively low number of Mks in the lungs and the time required for fragmentation to occur (Lefrançois et al., 2017), in the wild-type mouse, proPlt formation alone cannot account for the number of Plts required to maintain the steady-state Plt mass (Table S6, Table S7, and Table S8). Although visualization of membrane bud formation and release was conclusively observed in FL explants, due to current technological constraints (z-stack acquisition rates) we are unable to track released membrane buds into the peripheral circulation of adult mice. Accordingly, our estimate of Plt production via membrane budding in the adult has the caveat that the rate of membrane bud release is assumed to be equal to the rate of membrane bud formation.

We did not observe Plt release directly from proPlts in the BM. However, we cannot discount the possibility that this process occurs in the peripheral circulation (Thon et al., 2012); the extent to which this contributes to the circulating Plt mass

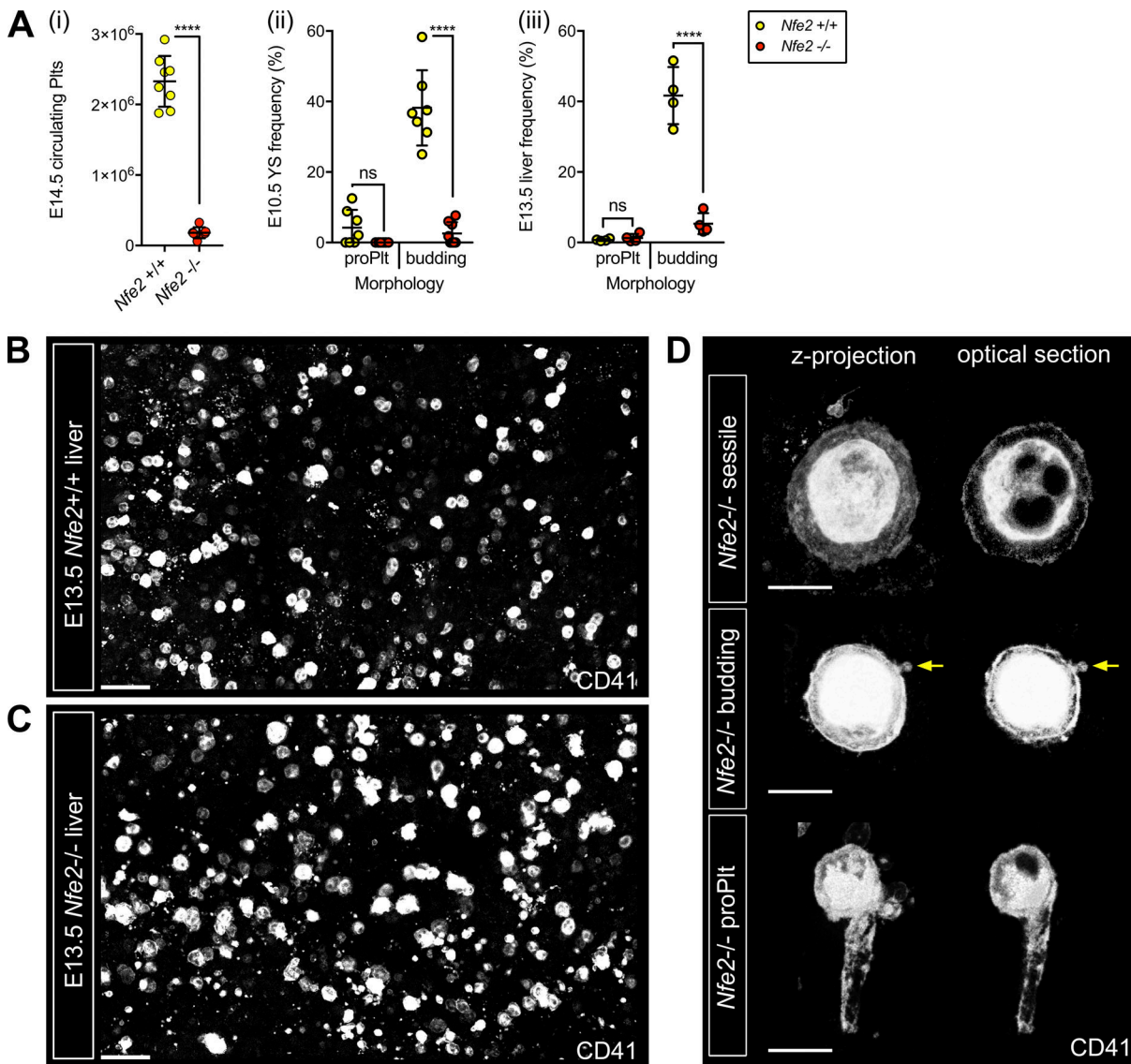


Figure 8. Fetal $Nfe2^{-/-}$ Mks fail to produce plasma membrane buds. (Ai) E14.5 $Nfe2^{+/+}$ ($n = 8$ mice) and $Nfe2^{-/-}$ ($n = 7$ mice) circulating Plt counts. **(Aii and Aiii)** In situ Plt-forming morphologies in the E10.5 YS (ii, $Nfe2^{+/+}$, $n = 7$ mice; $Nfe2^{-/-}$, $n = 8$ mice) and E13.5 FL (iii, $Nfe2^{+/+}$, $n = 4$ mice; $Nfe2^{-/-}$, $n = 4$ mice). **(B and C)** Representative 3D z-projections of Mks in $Nfe2^{+/+}$ (B, $n = 4$ mice) and $Nfe2^{-/-}$ (C, $n = 4$ mice) E13.5 FLs (CD41, gray). Scale bars, 100 μ m. **(D)** Representative examples of $Nfe2^{-/-}$ sessile, budding, and proPlt forming Mks in z-projection and optical section. Arrow indicates a membrane bud. Scale bars, 20 μ m.

would require experimental clarification. Given the high rate of Plt production via budding that was observed in vivo, approaches to produce sufficient Plts for cost-effective clinical use would be greatly enhanced by identifying conditions that promote sustained membrane budding.

Our findings indicate that the cellular mechanism of Plt formation is exquisitely sensitive to the environment. In vitro, the vast majority of Mks form proPlts. However, in vivo we observed a different outcome: the majority of in vivo Mks undergo membrane budding. The idea of context dependence is supported by our observations from $Nfe2^{-/-}$ mice: $Nfe2^{-/-}$ FL-derived Mks have been reported to be defective in their ability to generate proPlts in vitro (Lecine et al., 1998). In contrast, our data (which represent the first exploration of the in vivo behavior of $Nfe2^{-/-}$ Mks) indicate that NF-E2 is dispensable for

in vivo proPlt formation but is critical for membrane budding. Although we show that the formation, release, and fragmentation of proPlts occur in the absence of NF-E2 in vivo, we cannot be certain that the severe loss of circulating Plts in $Nfe2^{-/-}$ mice is attributable to the loss of membrane budding alone.

We observed that in addition to the possibility that in vivo proPlts give rise to Plts, and consistent with the observations of others (Brown et al., 2018; Lefrançois et al., 2017), proPlt formation was associated with the exit of Mks from the BM space via a diapedesis-like process; this could result in the reported seeding of BM-derived Mks within the intravascular spaces of the lungs (Lefrançois et al., 2017). It will be of interest to determine whether membrane budding and proPlt formation do indeed represent alternative mechanisms of Plt production or whether in vivo proPlt formation is associated with other facets of Mk biology.

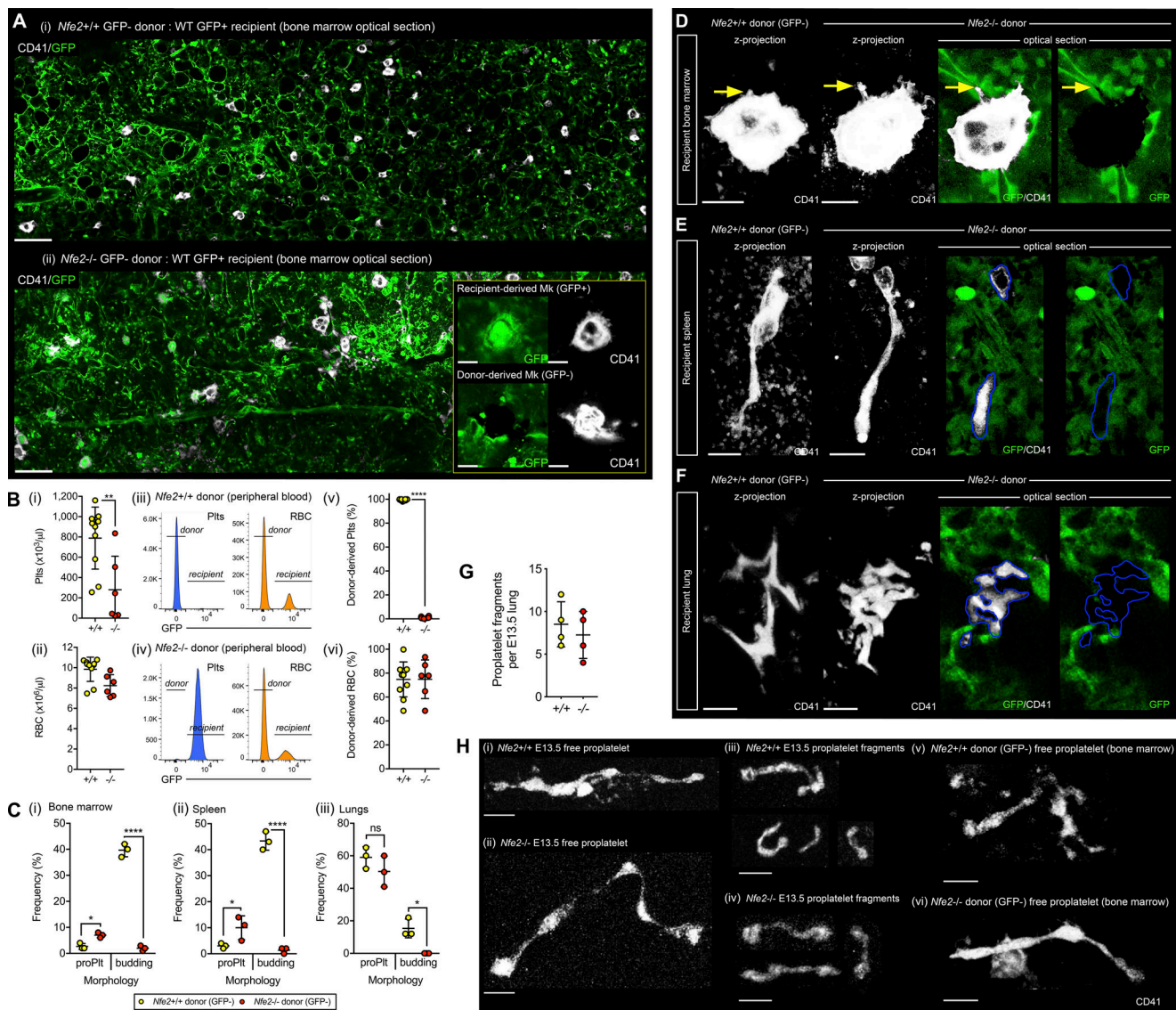


Figure 9. *Nfe2^{-/-}* Mks in the ABM generate proPlts but exhibit a failure of membrane budding. (A) Representative examples of optical sections from chimeric BM (femoral) harvested from recipients of *Nfe2^{+/+}* (i, *n* = 3 mice) and *Nfe2^{-/-}* (ii, *n* = 3 mice) donor E13.5 FLs. GFP⁻ donor-derived Mks are readily distinguished from recipient GFP⁺ cells (including Mks) according to GFP expression (ii, inset). Scale bars, 100 μm. (B) Total Plts (i) and RBC (ii) counts in recipients of *Nfe2^{+/+}* (*n* = 10 mice) and *Nfe2^{-/-}* (*n* = 6 mice) E13.5 FL 4–5 wk after transplantation. For i, *P* = 0.007, two-tailed unpaired *t* test. Detection (iii–iv) and quantification (v–vi) of donor-derived (GFP⁻) Plts and RBCs. For v, *P* < 0.0001, two-tailed unpaired *t* test. (C) Frequency of observed donor (GFP⁻) *Nfe2^{+/+}* and *Nfe2^{-/-}* Mk morphologies within the BM (i), spleen (ii), and lungs (iii) of recipient mice (*n* = 3 mice per donor genotype); ****, *P* < 0.0001 and *, *P* = 0.04, one-way ANOVA with Sidak’s correction (i); ****, *P* < 0.0001 and *, *P* = 0.18, one-way ANOVA with Sidak’s correction (ii); *, *P* = 0.04, one-way ANOVA with Sidak’s correction (iii). (D–F) Representative examples of donor-derived (GFP⁻) *Nfe2^{+/+}* and *Nfe2^{-/-}* Mks budding in the BM (D) and undergoing proPlt formation in the spleen (E) and lungs (F). Scale bars, 20 μm. Yellow arrow indicates membrane bud, blue outline highlights proPlt-forming Mks; *n* = 3 replicates per donor genotype. (G) Quantification of proPlt fragments within the vasculature of lungs of *Nfe2^{+/+}* and *Nfe2^{-/-}* fetuses. *n* = 4 independent experiments. *P* = 0.53, two-tailed unpaired *t* test. (H) Representative examples of free proPlts in the peripheral circulation of E13.5 *Nfe2^{+/+}* (i) and *Nfe2^{-/-}* (ii) mice. Representative examples of free proPlt fragments in the peripheral circulation of E13.5 *Nfe2^{+/+}* (iii) and *Nfe2^{-/-}* (iv) mice that are consistent in shape and size with proPlt fragments. Data are representative of eight independent experiments. Representative examples of free proPlts that were present in the BM of GFP⁺ adult mice that had been reconstituted with GFP⁻ *Nfe2^{+/+}* cells (v) and GFP⁻ *Nfe2^{-/-}* cells (vi). *n* = 4 independent experiments. Scale bars, 10 μm.

Materials and methods

Mice

Pf4-Cre (Tiedt et al., 2007), *Nfe2^{-/-}* (Shivdasani et al., 1995), *Flk1-GFP* (Jakobsson et al., 2010), YFP reporter (Srinivas et al., 2001), and mTmG mice (Muzumdar et al., 2007) were maintained on a C57BL/6 background, and *R26R-Confetti* (Snippert et al., 2010) on a 129/Sv background. Experimental procedures were approved by the Walter and Eliza Hall Institute Animal Ethics Committee.

Developmental stages were determined morphologically by Theiler’s criteria. Timed matings were set up overnight, with the morning of a positive plug designated E0.5. All adult experimental mice were females 10–16 wk of age.

Embryonic tissue collection

Embryos were dissected in prewarmed Dulbecco’s PBS (DPBS) with 7% FCS to isolate yolk sac or FL. Single-cell suspensions

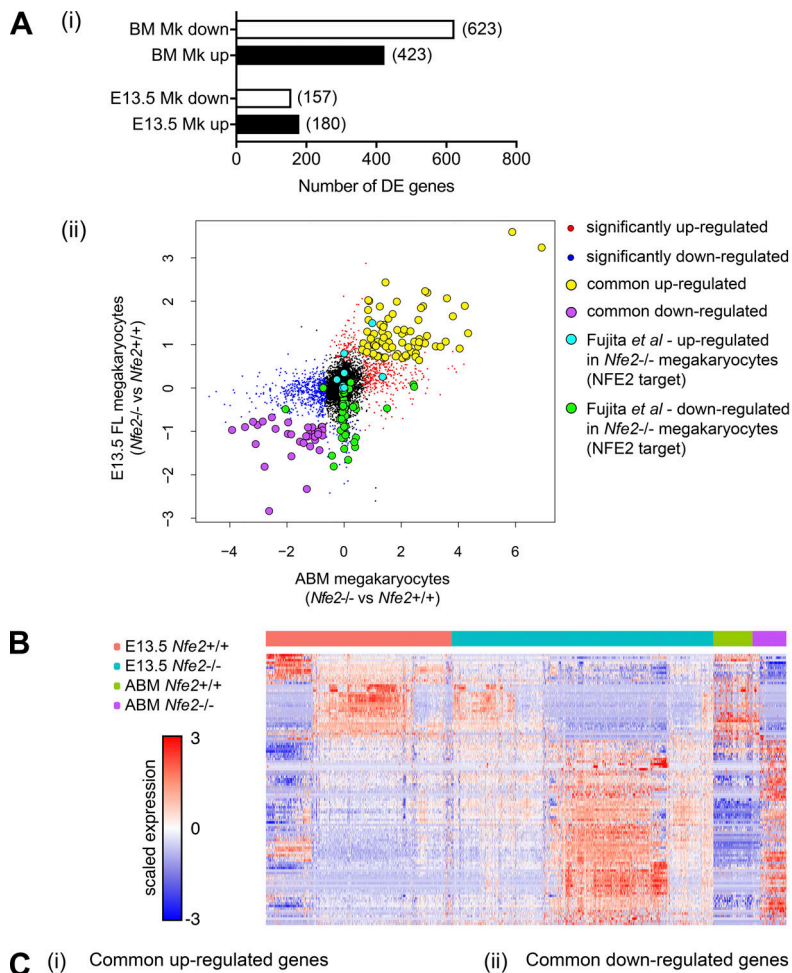


Figure 10. Identification of genes correlated with loss of membrane budding in the FL and ABM. **(Ai)** Summary of up-regulated and down-regulated DE genes in comparisons of E13.5 FL *Nfe2^{+/-}* versus *Nfe2^{-/-}* Mks, and ABM *Nfe2^{+/-}* versus *Nfe2^{-/-}* Mks. All DE genes are listed in Data S1 and Data S2. **(Aii)** Scatter plot of *Nfe2^{+/-}* versus *Nfe2^{-/-}* Mk gene expression log₂ fold change from E13.5 FL and ABM sc RNA-seq. Highlighted are genes identified as significantly up-regulated (red) or down-regulated (blue); commonly up-regulated (yellow) or down-regulated (purple) at both developmental stages; and NFE2 direct target genes that are up-regulated (cyan) and down-regulated (green) in FL culture-derived *Nfe2^{-/-}* Mks (Fujita *et al*, 2013). **(B)** Heatmap of all common significantly DE genes. Rows were hierarchically clustered using 1 - Person correlation. **(C)** Complete list of enriched GO biological process terms for commonly up-regulated genes (i) and selected enriched GO biological process terms for commonly down-regulated genes (ii). See Table S5 for a complete list of enriched GO terms and Materials and methods for details of statistical analysis.

were generated by incubating tissues in 10% collagenase and dispase (Roche) for 45 min at 37°C, washing, and manually dissociated by trituration. FLs were manually dissected into cross sections using sharpened tungsten needles. Peripheral blood was collected from individual embryos in prewarmed calcium- and magnesium-free DPBS with 7% FCS and EDTA as previously described (Potts *et al*, 2015).

ProPlt-forming assay

Either single-cell suspensions from whole FL or purified CD41^{high}CD45⁻ cells from the yolk sac were cultured in defined serum-free medium (Norol *et al*, 1998) with 100 ng/ml recombinant murine thrombopoietin (Peprotech) for ≤3 d at 37°C with 5% CO₂.

3D confocal microscopy

Yolk sacs were fixed in 2% paraformaldehyde (PFA) for 20 min at room temperature; FLs were fixed in 2% PFA with 0.1%

Tween-20 for 1 h at room temperature, sliced, blocked, and permeabilized in 10% FCS/0.6% Triton X-100. For GFP detection, samples were first stained with a purified chicken anti-GFP antibody and then with an anti-chicken-Alexa Fluor 488 antibody. Antibody staining steps were performed overnight at 4°C (antibodies listed in Table S8) with wash steps at room temperature over 2–4 h. Nuclei were visualized with DAPI. All liver samples were cleared in a glycerol gradient (5–80%) before confocal imaging. Images were captured using a Zeiss LSM780 inverted confocal microscope with a 40× oil-immersion objective lens. A pixel resolution of 1,024 × 1,024 was used with 2× averaging and laser power depth correction.

After dissection, ABM and spleen were fixed overnight in 4% PFA at 4°C. Lungs were inflated using either 4% PFA or 1.75% agarose, immersed in 4% PFA, and fixed overnight at 4°C. Bones were decalcified in 0.5 M EDTA, 4°C (Kusumbe *et al*, 2015). All samples were embedded in low-melting-temperature agarose

(3%). A Leica VT1000 S vibratome was used to generate 250- μm sections of each tissue. After antibody staining (as above), data were acquired using a Zeiss LSM880 upright confocal microscope using λ scanning and spectral unmixing. Four to six full-length sections were used from each sample; samples were collected from three independent mice. Data from all samples were acquired using a 10 \times air objective lens and a 40 \times oil-immersion objective lens. A pixel resolution of 1,024 \times 1,024 was used with laser power depth correction. Images were analyzed using Imaris 9 (Bitplane) and Prism 7 (GraphPad) software.

FL 4D confocal microscopy

E13.5 liver slices were incubated in serum-free medium (Norol et al., 1998) with anti-CD41 (allophycocyanin conjugated) antibody at 37°C with 5% CO₂ overnight to allow optimal antibody loading. Slices were transferred to glass-bottom 35-mm dishes (Ibidi) in fresh preacclimatized medium and overlaid with embryo culture-grade mineral oil (Sigma-Aldrich) for imaging. The Z-stack acquired was ~50–80 μm ; start and end positions were restricted to regions within the explanted organ; and cells on the coverslip were not included in the imaged region. Z-stacks were acquired every 3–5 min using a 633-nm laser for ≤ 15 h (in a humidified chamber at 37°C and 5% CO₂) using a Leica SP8 microscope equipped with a high-resonance scanner. Data were captured at a 512 \times 512-pixel resolution. Data presented are derived from eight independent experiments.

ABM 4D intravital microscopy

Using either *Pf4-Cre:YFP* or *Pf4-Cre:mTmG* mice, intravital microscopy was performed with an Olympus FVMPE-RS two-photon upright microscope equipped with a motorized stage, two tunable infrared multiphoton lasers (Spectraphysics INSIGHT X3-OL 680–1,300-nm laser and Mai Tai HPDS-OL, 690–1,040-nm), and a resonance scanner. The signal was visualized with an Olympus FV30-AC25W 25 \times magnification water-immersion lens (1.05 NA) and nondescanned detectors. Collagen bone second harmonic generation (SHG) signal, Cy-5, Tomato, YFP, and GFP signals were detected as follows: excitation 1,125 nm – 660–750-nm emission (Cy-5); excitation 1,050 nm – 560–679-nm emission (Tomato); excitation 860 nm – 500–550-nm (YFP or GFP) or 415–485-nm (SHG) emission. For surgery, anesthesia was induced in mice with 5% isoflurane mixed with pure oxygen. This was gradually reduced to ~2% as anesthesia stabilized. Surgery to attach the headpiece and imaging was performed as described previously (Hawkins et al., 2016). When required, vasculature was labeled by intravenous injection of 50 μl of 8 mg/ml 500-kD Cy5 Dextran (Nanocs). Acquired images were processed using Imaris (Bitplane) or Fiji/ImageJ (National Institutes of Health).

Analysis of *Pf4-Cre:Confetti* FL

Transient expression of Cre in a diploid cell harboring one copy of the *Confetti* construct results in stable expression of nuclear GFP (nGFP), cytoplasmic YFP (cYFP), membrane CFP (mCFP), or cytoplasmic RFP (cRFP). *Pf4-Cre* is continuously expressed in Mks, so the diversity of colors per Mk is reduced owing to repeated cassette inversion, but generating four resolvable *Confetti* configurations: (a) no recombination (no fluorescence); (b) expression of cassette 1 (nGFP and cYFP); (c) expression of cassette

2 (cRFP and mCFP); and (d) activation in polyploid Mks (which harbor at least two *Confetti* copies) resulted in expression of both cassettes 1 and 2, (nGFP, cYFP, cRFP, and mCFP). Configurations (a) through (d) were distinguishable by microscopy using an antibody against GFP derivatives (nGFP, cYFP, and mCFP) and an antibody against cRFP. Because Plts are anucleate cells, expression of cassette 1 was determined by cYFP expression alone. mCFP was not detectable following sample preparation; thus, cRFP was used to identify cassette 2 expression.

Quantitative analysis of imaging data

Only complete volumes of Mks and Plts were used for 3D and 4D data: any truncated cells were eliminated from further analysis. For 4D data, Mks within the imaging region for <1 h were excluded from analyses; annotation of tracks was stopped once the target cell migrated out of the field of view. ProPlts were defined as pseudopodial extensions that were equal to or greater than the diameter of the attached Mk. Surface objects for Mks and Plts were based on CD41 expression; nuclei surface objects were based on DAPI staining. The values for the relevant parameters were extracted from surface objects using Imaris software, exported as an Excel file, and processed in Prism software.

For both ex vivo FL and in vivo ABM 4D imaging, membrane buds were identified by interrogating both the z-projection and all z-positions within each frame. As shown in Fig. S3, buds were distinguished from passing Plts by the presence of structural continuity between the putative bud and Mk. This conservative approach likely resulted in the underestimation of the number of released Plts via budding, but eliminated the possibility of false-positive calls.

Electron microscopy

Lobes from E13.5 FL were fixed at room temperature for 3–4 h in 2% PFA/2.5% glutaraldehyde/0.1 M sodium cacodylate buffer (pH 7.4), postfixed in 2% osmium tetroxide/0.1 M sodium cacodylate buffer, dehydrated through a graded series of ethanol, and then washed twice in 100% acetone. For transmission electron microscopy, dehydrated livers were infiltrated overnight in Spurr's resin. Ultrathin sections were cut with a diamond knife (Diatome) on a Leica Ultracut 7 ultramicrotome (Leica Microsystems) and picked up on copper grids. Sections were contrasted with methanolic saturated uranyl acetate and Reynold's lead citrate. Images were captured using a JEOL 1011 TEM microscope. For scanning electron microscopy, after fixation and ethanol dehydration, lobes were fractured at room temperature followed by critical point drying. Liver pieces were returned to 100% ethanol and critical point dried (Leica EM CPD 300). Samples were then mounted on an aluminum stub, sputter coated in gold (Emscope sc500 gold sputter coater), and stored in a desiccator until imaged. A second gold sputter coat was applied immediately before image acquisition if charging had occurred. Images were captured on a JEOL NeoScope II SEM (Coherent Scientific).

Flow cytometry

Single-cell suspensions were stained for 1 h on ice with combinations of antibodies as in Table S1; peripheral blood samples were stained for 20 min at room temperature. 7-Aminoactinomycin D (7AAD; Thermo Fisher Scientific) was used for viability

discrimination. *R26R-Confetti* FL Mk and peripheral blood Plt samples were analyzed individually with 7AAD and anti-CD41, and then for expression of RFP, CFP, and GFP/YFP (detected in the same filter channel). Ploidy analysis samples were prepared as follows: single-cell suspensions were stained as above, then fixed in ice-cold 70% ethanol for 1 h, washed, and resuspended in 0.1% Triton X-100/0.5% DAPI/calcium- and magnesium-free DPBS.

Confetti MEFs

MEFs were derived from *R26R-Confetti/+* E13.5 embryos and passaged twice before cryopreservation. After recovery, MEFs at 50% confluence were treated with TAT-Cre (10 μ M; generated in-house) for 5 h to induce *Confetti* recombination, then expanded for 8 d before purifying populations by flow cytometry. Cells were cytospun onto polylysine-coated slides, fixed with 2% PFA, and stained with anti-GFP and anti-RFP antibodies and DAPI as used in the whole-mount *Pf4-Cre:Confetti* imaging.

Apoptotic active CASPASE-3 assay

Mks were analyzed in E13.5 FL slices by confocal microscopy for expression of cleaved active CASPASE-3 as a marker of apoptosis. As a positive control, liver slices were cultured in IMDM with 10% FCS, 0.1% β -mercaptoethanol, 1% L-glutamine, and penicillin/streptomycin, supplemented with 4 μ M Camptothecin (Sigma-Aldrich; C9911) for 4 h at 37°C with 5% CO₂. After fixation in 2% PFA with 0.1% Tween20 for 1 h, slices were processed as above and stained with anti-CD41 and anti-active CASPASE-3 antibodies. Slices were cleared using a glycerol gradient before confocal imaging on Zeiss LSM780 confocal as above.

Adult tissue cellularity, Mk number, and circulating Plt number estimations

After removal of soft tissue, marrow was harvested from the following bones by crushing: all long bones (two femurs, two tibias, two radii, and two humeri), spine, pelvis, ribs and sternum, and skull. Cell suspensions of spleen were produced by crushing. Cell suspensions of lung were produced as previously described (Lefrançois et al., 2017). Absolute cell counts were determined using a hemocytometer, only cells excluding eosin were scored. The frequency of BM cells was determined using flow cytometry via the exclusion of small cells (to reduce contamination by peripheral blood) and 7AAD⁺ events. Mks were identified according to a TER119⁻CD41^{high}CD150⁺ immunophenotype. Values from flow cytometric analysis and hemocytometer counts were used to determine total Mk numbers. Adult peripheral blood was analyzed using an ADVIA blood counter, from which Plt concentration was determined (cells per liter); these values were adjusted to a previously described estimate of total blood volume per mouse (2.3 ml; Barbee et al., 1992).

Hematopoietic chimera generation

Livers from five GFP⁻ E13.5 *Nfe2^{+/+}* or GFP⁻ *Nfe2^{-/-}* embryos were mechanically dissociated and transplanted into lethally irradiated (2 \times 5 Gy) UBC-GFP⁺ recipients (0.38 embryo equivalents per recipient). Mice were screened at 4 wk for hematopoietic recovery (ADVIA) and GFP status (flow cytometry).

Single-cell RNA sequencing (scRNA-seq)

Livers from eight E13.5 wild-type and six *Nfe2^{-/-}* embryos were dissected, mechanically dissociated, filtered, and pooled by genotype. Samples were stained for CD41, CD42d, LIN (Ter119, B220), LIN⁻ CD41^{high} CD42d⁺ Cells were sorted on an Aria Cell Sorter (Becton Dickinson), centrifuged, and counted. From hematopoietic chimeras that had received either wild-type or *Nfe2^{-/-}* E13.5 livers, BM from the femurs, tibias, hips, and humeri were collected, pooled by genotype. Donor derived Mks were purified by flow cytometry according to a GFP⁻Ter119⁻B220⁻ CD41^{high} CD42d⁺ immunophenotype; after purity analysis and cell counting, collected cells were loaded into a Chromium Controller (10X Genomics; Table S4). Single cell 3' v2 transcriptome libraries were obtained following manufacturer's instructions and sequenced on NextSeq (Illumina; 75 bp, paired end).

Bioinformatics analysis

FL Mks were purified from eight E13.5 *Nfe2^{+/+}* and six *Nfe2^{-/-}* embryos. ABM Mks were collected from hematopoietic chimeras and pooled by genotype. Samples were stained for CD41, CD42D, Ter119, and B220; TER119⁻B220⁻CD41^{high}CD42D⁺ cells were purified by flow cytometry. Single-cell 3' libraries were generated using the Chromium platform (10X Genomics). Each sample was sequenced to 79–91% saturation. Genes detected in <10 cells were excluded. Adult samples were sequenced to ~200 million reads and embryonic samples to ~650 million reads, an average read depth of 150,000–210,000 reads/cell. Reads were processed using the 10X Genomics Cell Ranger Single Cell 2.2.0 pipeline as previously described (Zheng et al., 2017). Samples were split by genotype and developmental stage using indexes and then FASTQs generated from Illumina sequencing output were aligned to the reference genome using the STAR algorithm. Gene-barcode matrices were generated for each individual sample by counting unique molecular identifiers and filtering noncell-associated barcodes. This was then imported into the Seurat (v1.4.0.15) R toolkit for quality control and downstream analysis of our scRNA-seq experiment (Fig. S5; Macosko et al., 2015). All functions were run with default parameters, unless specified otherwise. Gene expression was log normalized to a scale factor of 10,000.

Hematopoietic lineage signatures were generated from Haemopedia mouse RNA-seq (Choi et al., 2019), using the top 100 (after removal of T cell receptor and Ig variants) genes for each of 13 lineages as defined in the collection, using the High Expression Search function at <https://www.haemosphere.org/searches>. Expression of signatures was compared with a competitive gene set test using Camera (Wu and Smyth, 2012). The most positively up-regulated signature was assigned to each cluster as its lineage (Fig. S5). One mutant embryonic cluster was assigned as erythrocytic but also scored high for the Mk signature. These cells were included as Mks for further differential expression analysis. The cells remaining were 170 *Nfe2^{+/+}* and 147 *Nfe2^{-/-}* ABM Mks; 805 *Nfe2^{+/+}* and 1,138 *Nfe2^{-/-}* E13.5 liver Mks (including 420 with erythrocyte character).

For differential expression analysis, counts were converted to log₂ counts per million, quantile normalized, and precision weighted with the “voom” function of the limma package (Law et al., 2014). A linear model was fitted to each gene, and

empirical Bayes moderated *t* statistics were used to assess differences in expression (Ritchie et al., 2015). Empirical Bayes moderated-*t* P values were computed relative to a fold-change cutoff of 0.5-fold using *treat* (McCarthy and Smyth, 2009). P values were adjusted to control the global false discovery rate across all comparisons with the “separate” option of the *limma* package, and genes of interest were selected that were found to be DE in the same direction in both comparisons. Data have been made available through NCBI’s GEO (Edgar et al., 2002) under accession GSE125579. For gene ontology analysis, genes that were identified as up- or down-regulated in both E13.5 and ABM *Nfe2^{-/-}* Mks were entered into the Panther portal at <http://geneontology.org/page/go-enrichment-analysis>. Heatmaps were generated using Morpheus software. Where indicated, hierarchical clustering was performed using the “1 minus Person correlation” metric. Functional annotation of significantly DE genes was performed using the Panther portal (<http://pantherdb.org/>). Gene sets that are bound by NF-E2 and DE in in vitro cultures of E13.5-derived *Nfe2^{-/-}* Mks were derived from Table S2 in Fujita et al. (2013). They were tested for differential expression in our primary sourced *Nfe2^{-/-}* Mks using Fry rotation gene set test (Wu et al., 2010) in the *limma* R/Bioconductor (Ritchie et al., 2015) software package.

Estimation of the systemic rate of Plt replacement and Plt production

Total number of Plts per mouse was determined by the sum of the number of circulating Plts (Fig. S4 C) and the number expected to be sequestered in the spleen (one third of total):

$$\begin{aligned} \text{Total platelets per mouse} &= \text{circulating platelets} + \\ &\text{one third in spleen} \\ &= 2.9 \times 10^9 + 1.45 \times 10^9 \\ &= 4.35 \times 10^9 \text{ platelets.} \end{aligned}$$

The Plt production rate required to maintain normal numbers of circulating Plts was determined by dividing the total Plt number per mouse by the time required for the replacement of all circulating Plts (114 h; Dowling et al., 2010; Mason et al., 2007):

$$\begin{aligned} \text{Platelets required per hour} &= \left(\frac{\text{total platelets}}{\text{total replacement time}} \right) \\ &= \frac{4.35 \times 10^9 \text{ platelets}}{114 \text{ hours}} \\ &= 3.82 \times 10^7. \end{aligned}$$

The total number of sessile (non-proPlt-forming) Mks from all major BM sites, spleen, and lungs was calculated by multiplying the total number of Mks in each tissue by the fraction of “budding” and “nothing” cells (Fig. 6, C, E-G, and I):

$$\begin{aligned} \text{Sessile marrow megakaryocytes} &= 336,358 \times \left(\frac{99}{100} \right) \\ &= 332,994 \text{ cells.} \end{aligned}$$

The total number of potential budding Mks in the BM was determined by multiplying the total number of sessile Mks by the fraction of observed budding Mks in the calvarial marrow (84%; Fig. 5 J):

$$\begin{aligned} \text{Budding marrow megakaryocytes} &= 332,994 \times \left(\frac{84}{100} \right) \\ &= 279,715 \text{ cells.} \end{aligned}$$

The potential Plt production rate (per hour) by budding Mks in the BM was determined by multiplying the total number of budding Mks by the observed Plt release rate per minutes (2 per minute; Fig. 5 L) multiplied by 60 min:

$$\begin{aligned} \text{Marrow platelet production} &= \\ &(234,960 \text{ cells} \times 2 \text{ per min}) \times 60 \text{ min} \\ &= 3.4 \times 10^7 \text{ platelets per h.} \end{aligned}$$

General statistical analyses

Prism 7 (GraphPad) was used for data analysis and graph production. Data are presented as mean \pm SD and were analyzed using Student’s *t* test (two-way, unpaired). One-way ANOVA (using Tukey’s P value adjustment) was used for multiple comparisons. Differences were considered statistically significant when $P < 0.05$; designation of ns indicates differences were not significant. *, $P < 0.05$; **, $P < 0.01$; ***, $P < 0.001$; ****, $P < 0.0001$. For the comparison of Plt formation and Mk ploidy, contingency analysis was performed using the two-tailed χ^2 test; $P > 0.05$ was considered not significant. *n* was used to designate the number of independent experiments, and *o* for the number of observations.

Online supplemental material

Fig. S1 shows validation of in situ ploidy quantification in the E13.5 FL from high-volume 3D imaging data. Fig. S2 shows validation of the *Pf4-Cre:Confetti* system to determine the origin of Mk membrane buds. Fig. S3 shows the criteria used for membrane bud identification in *Pf4-Cre:YFP* ABM. Fig. S4 shows the cellularity and Mk abundance in major Mk-containing adult organs. Fig. S5 shows the scRNA-seq quality control metrics and lineage assignment used. Video 1 illustrates the conversion of high-volume 3D images of the E13.5 FL into quantifiable datasets. Video 2 demonstrates that ex vivo proPlt formation is rare but can occur from Mks during E13.5 FL organotypic culture. Video 3 demonstrates that direct release of membrane buds occurs within the E13.5 FL environment without engaging proPlt formation. Video 4 shows an E13.5 FL Mk budding directly into the peripheral circulation. Video 5 shows an example of the large-scale 4D whole calvarial BM imaging datasets produced using multiphoton intravital imaging. Video 6 demonstrates that proPlt formation in the BM is a slow process. Video 7 shows that thick extensions from Mks with complex morphology do not produce proPlts. Video 8 shows three examples of Mks undergoing membrane budding in the ABM. Video 9 shows an Mk exiting from the BM space after proPlt formation. Table S1 shows the antibodies/protein detection reagents used in this study. Table S2 shows the metrics associated with generation of Mk scRNA-seq data. Table S3 shows commonly down-regulated genes in *Nfe2^{-/-}* Mks versus *Nfe2^{+/+}* Mks. Table S4 shows commonly up-regulated genes in *Nfe2^{-/-}* Mks versus *Nfe2^{+/+}* Mks. Table S5 is the complete list of GO biological process terms enriched from commonly down-regulated genes in *Nfe2^{-/-}* Mks

versus *Nfe2^{+/+}* Mks. Table S6 shows a summary of base values used to estimate Plt production. Table S7 shows the parameters used to estimate potential Plt yield from BM and lung Mks. Table S8 shows the comparison of Plt production via proPlt formation and membrane budding. Data S1 lists some of the different genes used. Data S2 lists the remaining genes used.

Acknowledgments

We thank Dr. Julie Sheridan and Professor Marnie Blewitt for critical comments on the manuscript and Dr. Sarah Best for assistance with lung experiments. We are grateful to Professor Alexander Medvinsky (Centre for Regenerative Medicine, Edinburgh, UK) and Dr. Kelly Rogers (Walter and Eliza Hall Institute, Melbourne, Australia) for discussions and generous provision of reagents, and to Associate Professor Sarah Ellis for assistance with electron microscopy. Next-generation sequencing was performed by Dr. Stephen Wilcox at the Ian Potter Centre for Genomics within the Walter and Eliza Hall Institute.

This work was supported by the Australian Research Council Stem Cells Australia program, National Health and Medical Research Council project (1128993, 1129012) and Program (1113577) grants, and Independent Research Institutes Infrastructure Support Scheme from the National Health and Medical Research Council (grant 361646), the Australian Cancer Research Foundation, and State Government of Victoria Operational Infrastructure Support. E.D. Hawkins and W.S. Alexander were supported by National Health and Medical Research Council fellowships; K.S. Potts by an Australian Research Council Strategic Research Australian Postgraduate Award studentship; and E.C. Josefsson by a fellowship from the Lorenzo and Pamela Galli Charitable Trust.

Author contributions: K.S. Potts, A. Farley, C.A. Dawson, J. Rimes, C. Biben, C. de Graaf, O.J. Stonehouse, A. Carmagnac, C. Anttila, D. Amann-Zalcenstein, S. Naik, M.A. Potts, P. Gangatirkar, E.C. Josefsson, W.S. Alexander, D.J. Hilton, and E.D. Hawkins designed and/or performed experiments and analyzed data; S. Taoudi conceived the study, designed and performed experiments, and analyzed data. All authors contributed to manuscript preparation.

Disclosures: The authors declare no competing interests exist.

Submitted: 21 November 2019

Revised: 16 March 2020

Accepted: 11 June 2020

References

Barbee, R.W., B.D. Perry, R.N. Ré, and J.P. Murgu. 1992. Microsphere and dilution techniques for the determination of blood flows and volumes in conscious mice. *Am. J. Physiol.* 263:R728–R733.

Becker, R.P., and P.P. De Bruyn. 1976. The transmural passage of blood cells into myeloid sinusoids and the entry of platelets into the sinusoidal circulation; a scanning electron microscopic investigation. *Am. J. Anat.* 145:183–205. <https://doi.org/10.1002/aja.1001450204>

Behnke, O. 1969. An electron microscope study of the rat megakaryocyte. II. Some aspects of platelet release and microtubules. *J. Ultrastruct. Res.* 26: 111–129. [https://doi.org/10.1016/S0022-5320\(69\)90039-2](https://doi.org/10.1016/S0022-5320(69)90039-2)

Brown, E., L.M. Carlin, C. Nerlov, C. Lo Celso, and A.W. Poole. 2018. Multiple membrane extrusion sites drive megakaryocyte migration into bone marrow blood vessels. *Life Sci. Alliance.* 1. e201800061. <https://doi.org/10.26508/lsa.201800061>

Chen, Z., M. Hu, and R.A. Shivdasani. 2007. Expression analysis of primary mouse megakaryocyte differentiation and its application in identifying stage-specific molecular markers and a novel transcriptional target of NF-E2. *Blood.* 109:1451–1459. <https://doi.org/10.1182/blood-2006-08-038901>

Choi, E.S., J.L. Nichol, M.M. Hokom, A.C. Hornkohl, and P. Hunt. 1995. Platelets generated in vitro from proplatelet-displaying human megakaryocytes are functional. *Blood.* 85:402–413. <https://doi.org/10.1182/blood.V85.2.402.402>

Choi, J., T.M. Baldwin, M. Wong, J.E. Bolden, K.A. Fairfax, E.C. Lucas, R. Cole, C. Biben, C. Morgan, K.A. Ramsay, et al. 2019. Haemopedia RNA-seq: a database of gene expression during haematopoiesis in mice and humans. *Nucleic Acids Res.* 47(D1):D780–D785. <https://doi.org/10.1093/nar/gky1020>

Delesque-Touchard, N., C. Pendaries, C. Volle-Challier, L. Millet, V. Salel, C. Hervé, A.M. Pflieger, L. Berthou-Soulie, C. Prades, T. Sorg, et al. 2014. Regulator of G-protein signaling 18 controls both platelet generation and function. *PLoS One.* 9. e113215. <https://doi.org/10.1371/journal.pone.0113215>

Dowling, M.R., E.C. Josefsson, K.J. Henley, P.D. Hodgkin, and B.T. Kile. 2010. Platelet senescence is regulated by an internal timer, not damage inflicted by hits. *Blood.* 116:1776–1778. <https://doi.org/10.1182/blood-2009-12-259663>

Duarte, D., E.D. Hawkins, O. Akinduro, H. Ang, K. De Filippo, I.Y. Kong, M. Haltalli, N. Ruivo, L. Straszowski, S.J. Vervoort, et al. 2018. Inhibition of Endosteal Vascular Niche Remodeling Rescues Hematopoietic Stem Cell Loss in AML. *Cell Stem Cell.* 22:64–77.e66.

Edgar, R., M. Domrachev, and A.E. Lash. 2002. Gene Expression Omnibus: NCBI gene expression and hybridization array data repository. *Nucleic Acids Res.* 30:207–210. <https://doi.org/10.1093/nar/30.1.207>

French, J.E. 1967. Blood platelets: morphological studies on their properties and life cycle. *Br. J. Haematol.* 13(s1):595–602. <https://doi.org/10.1111/j.1365-2141.1967.tb00767.x>

Fuentes, R., Y. Wang, J. Hirsch, C. Wang, L. Rauova, G.S. Worthen, M.A. Kowalska, and M. Poncz. 2010. Infusion of mature megakaryocytes into mice yields functional platelets. *J. Clin. Invest.* 120:3917–3922. <https://doi.org/10.1172/JCI43326>

Fujita, R., M. Takayama-Tsujimoto, H. Satoh, L. Gutiérrez, H. Aburatani, S. Fujii, A. Sarai, E.H. Bresnick, M. Yamamoto, and H. Motohashi. 2013. NF-E2 p45 is important for establishing normal function of platelets. *Mol. Cell. Biol.* 33:2659–2670. <https://doi.org/10.1128/MCB.01274-12>

Gekas, C., K.E. Rhodes, L.M. Gereige, H. Helgadottir, R. Ferrari, S.K. Kurdistani, E. Montecino-Rodriguez, R. Bassel-Duby, E. Olson, A.V. Krivtsov, et al. 2009. Mef2C is a lineage-restricted target of Scf/Tall and regulates megakaryopoiesis and B-cell homeostasis. *Blood.* 113:3461–3471. <https://doi.org/10.1182/blood-2008-07-167577>

Hawkins, E.D., D. Duarte, O. Akinduro, R.A. Khorshed, D. Passaro, M. Nowicka, L. Straszowski, M.K. Scott, S. Rothery, N. Ruivo, et al. 2016. T-cell acute leukaemia exhibits dynamic interactions with bone marrow microenvironments. *Nature.* 538:518–522. <https://doi.org/10.1038/nature19801>

Hyun, Y.M., R. Sumagin, P.P. Sarangi, E. Lomakina, M.G. Overstreet, C.M. Baker, D.J. Fowell, R.E. Waugh, I.H. Sarelius, and M. Kim. 2012. Uropod elongation is a common final step in leukocyte extravasation through inflamed vessels. *J. Exp. Med.* 209:1349–1362. <https://doi.org/10.1084/jem.20111426>

Ihizumi, T., A. Hattori, M. Sanada, and M. Muto. 1977. Megakaryocyte and platelet formation: a scanning electron microscope study in mouse spleen. *Arch. Histol. Jpn.* 40:305–320. <https://doi.org/10.1679/aohc1950.40.305>

Italiano, J.E., Jr., P. Lecine, R.A. Shivdasani, and J.H. Hartwig. 1999. Blood platelets are assembled principally at the ends of proplatelet processes produced by differentiated megakaryocytes. *J. Cell Biol.* 147:1299–1312. <https://doi.org/10.1083/jcb.147.6.1299>

Ito, Y., S. Nakamura, N. Sugimoto, T. Shigemori, Y. Kato, M. Ohno, S. Sakuma, K. Ito, H. Kumon, H. Hirose, et al. 2018. Turbulence Activates Platelet Biogenesis to Enable Clinical Scale Ex Vivo Production. *Cell.* 174: 636–648.e18. <https://doi.org/10.1016/j.cell.2018.06.011>

Jakobsson, L., C.A. Franco, K. Bentley, R.T. Collins, B. Ponsioen, I.M. Aspalter, I. Rosewell, M. Busse, G. Thurston, A. Medvinsky, et al. 2010. Endothelial cells dynamically compete for the tip cell position during

- angiogenic sprouting. *Nat. Cell Biol.* 12:943–953. <https://doi.org/10.1038/ncb2103>
- Josefsson, E.C., C. James, K.J. Henley, M.A. Debrincat, K.L. Rogers, M.R. Dowling, M.J. White, E.A. Kruse, R.M. Lane, S. Ellis, et al. 2011. Megakaryocytes possess a functional intrinsic apoptosis pathway that must be restrained to survive and produce platelets. *J. Exp. Med.* 208: 2017–2031. <https://doi.org/10.1084/jem.20110750>
- Junt, T., H. Schulze, Z. Chen, S. Massberg, T. Goerge, A. Krueger, D.D. Wagner, T. Graf, J.E. Italiano, Jr., R.A. Shivdasani, et al. 2007. Dynamic visualization of thrombopoiesis within bone marrow. *Science*. 317: 1767–1770. <https://doi.org/10.1126/science.1146304>
- Kaufman, R.M., R. Airo, S. Pollack, and W.H. Crosby. 1965. Circulating megakaryocytes and platelet release in the lung. *Blood*. 26:720–731. <https://doi.org/10.1182/blood.V26.6.720.720>
- Koechlein, C.S., J.R. Harris, T.K. Lee, J. Weeks, R.G. Fox, B. Zimdahl, T. Ito, A. Blevins, S.H. Jung, J.P. Chute, et al. 2016. High-resolution imaging and computational analysis of haematopoietic cell dynamics in vivo. *Nat. Commun.* 7:12169. <https://doi.org/10.1038/ncomms12169>
- Kowata, S., S. Isogai, K. Murai, S. Ito, K. Tohyama, M. Ema, J. Hitomi, and Y. Ishida. 2014. Platelet demand modulates the type of intravascular protrusion of megakaryocytes in bone marrow. *Thromb. Haemost.* 112: 743–756. <https://doi.org/10.1160/TH14-02-0123>
- Kusumbe, A.P., S.K. Ramasamy, A. Starsichova, and R.H. Adams. 2015. Sample preparation for high-resolution 3D confocal imaging of mouse skeletal tissue. *Nat. Protoc.* 10:1904–1914. <https://doi.org/10.1038/nprot.2015.125>
- Lamkanfi, M., and V.M. Dixit. 2010. Manipulation of host cell death pathways during microbial infections. *Cell Host Microbe*. 8:44–54. <https://doi.org/10.1016/j.chom.2010.06.007>
- Law, C.W., Y. Chen, W. Shi, and G.K. Smyth. 2014. voom: Precision weights unlock linear model analysis tools for RNA-seq read counts. *Genome Biol.* 15:R29. <https://doi.org/10.1186/gb-2014-15-2-r29>
- Lecine, P., J.L. Villeval, P. Vyas, B. Swencki, Y. Xu, and R.A. Shivdasani. 1998. Mice lacking transcription factor NF-E2 provide in vivo validation of the proplatelet model of thrombocytopoiesis and show a platelet production defect that is intrinsic to megakaryocytes. *Blood*. 92:1608–1616. <https://doi.org/10.1182/blood.V92.5.1608>
- Lefrançois, E., G. Ortiz-Muñoz, A. Caudrillier, B. Mallavia, F. Liu, D.M. Sayah, E.E. Thornton, M.B. Headley, T. David, S.R. Coughlin, et al. 2017. The lung is a site of platelet biogenesis and a reservoir for haematopoietic progenitors. *Nature*. 544:105–109. <https://doi.org/10.1038/nature21706>
- Levin, J., J.P. Peng, G.R. Baker, J.L. Villeval, P. Lecine, S.A. Burstein, and R.A. Shivdasani. 1999. Pathophysiology of thrombocytopenia and anemia in mice lacking transcription factor NF-E2. *Blood*. 94:3037–3047. <https://doi.org/10.1182/blood.V94.9.3037>
- Macosko, E.Z., A. Basu, R. Satija, J. Nemes, K. Shekhar, M. Goldman, I. Tirosh, A.R. Bialas, N. Kamitaki, E.M. Martnersteck, et al. 2015. Highly Parallel Genome-wide Expression Profiling of Individual Cells Using Nanoliter Droplets. *Cell*. 161:1202–1214. <https://doi.org/10.1016/j.cell.2015.05.002>
- Mason, K.D., M.R. Carpinelli, J.I. Fletcher, J.E. Collinge, A.A. Hilton, S. Ellis, P.N. Kelly, P.G. Ekert, D. Metcalf, A.W. Roberts, et al. 2007. Programmed anuclear cell death delimits platelet life span. *Cell*. 128: 1173–1186. <https://doi.org/10.1016/j.cell.2007.01.037>
- McCarthy, D.J., and G.K. Smyth. 2009. Testing significance relative to a fold-change threshold is a TREAT. *Bioinformatics*. 25:765–771. <https://doi.org/10.1093/bioinformatics/btp053>
- Motohashi, H., M. Kimura, R. Fujita, A. Inoue, X. Pan, M. Takayama, F. Katsuoka, H. Aburatani, E.H. Bresnick, and M. Yamamoto. 2010. NF-E2 domination over Nrf2 promotes ROS accumulation and megakaryocytic maturation. *Blood*. 115:677–686. <https://doi.org/10.1182/blood-2009-05-223107>
- Muzumdar, M.D., B. Tasic, K. Miyamichi, L. Li, and L. Luo. 2007. A global double-fluorescent Cre reporter mouse. *Genesis*. 45:593–605. <https://doi.org/10.1002/dvg.20335>
- Nakamura, S., N. Takayama, S. Hirata, H. Seo, H. Endo, K. Ochi, K. Fujita, T. Koike, K. Harimoto, T. Dohda, et al. 2014. Expandable megakaryocyte cell lines enable clinically applicable generation of platelets from human induced pluripotent stem cells. *Cell Stem Cell*. 14:535–548. <https://doi.org/10.1016/j.stem.2014.01.011>
- Nishimura, S., M. Nagasaki, S. Kunishima, A. Sawaguchi, A. Sakata, H. Sakaguchi, T. Ohmori, I. Manabe, J.E. Italiano, Jr., T. Ryu, et al. 2015. IL-1 α induces thrombopoiesis through megakaryocyte rupture in response to acute platelet needs. *J. Cell Biol.* 209:453–466. <https://doi.org/10.1083/jcb.201410052>
- Norol, F., N. Vitrat, E. Cramer, J. Guichard, S.A. Burstein, W. Vainchenker, and N. Debili. 1998. Effects of cytokines on platelet production from blood and marrow CD34+ cells. *Blood*. 91:830–843. <https://doi.org/10.1182/blood.V91.3.830>
- Pertuy, F., A. Eckly, J. Weber, F. Proamer, J.Y. Rinckel, F. Lanza, C. Gachet, and C. Léon. 2014. Myosin IIA is critical for organelle distribution and F-actin organization in megakaryocytes and platelets. *Blood*. 123: 1261–1269. <https://doi.org/10.1182/blood-2013-06-508168>
- Potts, K.S., T.J. Sargeant, J.F. Markham, W. Shi, C. Biben, E.C. Josefsson, L.W. Whitehead, K.L. Rogers, A. Liakhovitskaia, G.K. Smyth, et al. 2014. A lineage of diploid platelet-forming cells precedes polyploid megakaryocyte formation in the mouse embryo. *Blood*. 124:2725–2729. <https://doi.org/10.1182/blood-2014-02-559468>
- Potts, K.S., T.J. Sargeant, C.A. Dawson, E.C. Josefsson, D.J. Hilton, W.S. Alexander, and S. Taoudi. 2015. Mouse prenatal platelet-forming lineages share a core transcriptional program but divergent dependence on MPL. *Blood*. 126:807–816. <https://doi.org/10.1182/blood-2014-12-616607>
- Radley, J.M., and C.J. Haller. 1982. The demarcation membrane system of the megakaryocyte: a misnomer? *Blood*. 60:213–219. <https://doi.org/10.1182/blood.V60.1.213.213>
- Radley, J.M., and M.A. Hartshorn. 1987. Megakaryocyte fragments and the microtubule coil. *Blood Cells*. 12:603–614.
- Reismann, D., J. Stefanowski, R. Günther, A. Rakhymzhan, R. Matthys, R. Nützi, S. Zehentmeier, K. Schmidt-Bleek, G. Petkau, H.D. Chang, et al. 2017. Longitudinal intravital imaging of the femoral bone marrow reveals plasticity within marrow vasculature. *Nat. Commun.* 8:2153. <https://doi.org/10.1038/s41467-017-01538-9>
- Renkawitz, J., A. Kopf, J. Stopp, I. de Vries, M.K. Driscoll, J. Merrin, R. Hauschild, E.S. Welf, G. Danuser, R. Fiolka, et al. 2019. Nuclear positioning facilitates amoeboid migration along the path of least resistance. *Nature*. 568:546–550. <https://doi.org/10.1038/s41586-019-1087-5>
- Ritchie, M.E., B. Phipson, D. Wu, Y. Hu, C.W. Law, W. Shi, and G.K. Smyth. 2015. limma powers differential expression analyses for RNA-seq and microarray studies. *Nucleic Acids Res.* 43. e47. <https://doi.org/10.1093/nar/gkv007>
- Schwer, H.D., P. Lecine, S. Tiwari, J.E. Italiano, Jr., J.H. Hartwig, and R.A. Shivdasani. 2001. A lineage-restricted and divergent beta-tubulin isoform is essential for the biogenesis, structure and function of blood platelets. *Curr. Biol.* 11:579–586. [https://doi.org/10.1016/S0960-9822\(01\)00153-1](https://doi.org/10.1016/S0960-9822(01)00153-1)
- Shivdasani, R.A., M.F. Rosenblatt, D. Zucker-Franklin, C.W. Jackson, P. Hunt, C.J. Sarris, and S.H. Orkin. 1995. Transcription factor NF-E2 is required for platelet formation independent of the actions of thrombopoietin/MGDF in megakaryocyte development. *Cell*. 81:695–704. [https://doi.org/10.1016/0092-8674\(95\)90531-6](https://doi.org/10.1016/0092-8674(95)90531-6)
- Snippert, H.J., L.G. van der Flier, T. Sato, J.H. van Es, M. van den Born, C. Kroon-Veenboer, N. Barker, A.M. Klein, J. van Rheenen, B.D. Simons, et al. 2010. Intestinal crypt homeostasis results from neutral competition between symmetrically dividing Lgr5 stem cells. *Cell*. 143:134–144. <https://doi.org/10.1016/j.cell.2010.09.016>
- Srinivas, S., T. Watanabe, C.S. Lin, C.M. Williams, Y. Tanabe, T.M. Jessell, and F. Costantini. 2001. Cre reporter strains produced by targeted insertion of EYFP and ECFP into the ROSA26 locus. *BMC Dev. Biol.* 1:4. <https://doi.org/10.1186/1471-213X-1-4>
- Strassel, C., M.M. Magiera, A. Dupuis, M. Batzenschlager, A. Hovasse, I. Pleines, P. Guéguen, A. Eckly, S. Moog, L. Mallo, et al. 2019. An essential role for α A-tubulin in platelet biogenesis. *Life Sci. Alliance*. 2. d201900309. <https://doi.org/10.26508/lsa.201900309>
- Takayama, M., R. Fujita, M. Suzuki, R. Okuyama, S. Aiba, H. Motohashi, and M. Yamamoto. 2010. Genetic analysis of hierarchical regulation for Gata1 and NF-E2 p45 gene expression in megakaryopoiesis. *Mol. Cell Biol.* 30:2668–2680. <https://doi.org/10.1128/MCB.01304-09>
- Thon, J.N., H. Macleod, A.J. Begonja, J. Zhu, K.C. Lee, A. Mogilner, J.H. Hartwig, and J.E. Italiano, Jr. 2012. Microtubule and cortical forces determine platelet size during vascular platelet production. *Nat. Commun.* 3:852. <https://doi.org/10.1038/ncomms1838>
- Thon, J.N., L. Mazutis, S. Wu, J.L. Sylman, A. Ehrlicher, K.R. Machlus, Q. Feng, S. Lu, R. Lanza, K.B. Neeves, et al. 2014. Platelet bioreactor-on-a-chip. *Blood*. 124:1857–1867. <https://doi.org/10.1182/blood-2014-05-574913>
- Thon, J.N., A. Montalvo, S. Patel-Hett, M.T. Devine, J.L. Richardson, A. Ehrlicher, M.K. Larson, K. Hoffmeister, J.H. Hartwig, and J.E. Italiano, Jr. 2010. Cytoskeletal mechanics of proplatelet maturation and platelet release. *J. Cell Biol.* 191:861–874. <https://doi.org/10.1083/jcb.201006102>
- Tiedt, R., T. Schomber, H. Hao-Shen, and R.C. Skoda. 2007. Pf4-Cre transgenic mice allow the generation of lineage-restricted gene knockouts for studying megakaryocyte and platelet function in vivo. *Blood*. 109: 1503–1506. <https://doi.org/10.1182/blood-2006-04-020362>
- Tober, J., A. Koniski, K.E. McGrath, R. Vemishetti, R. Emerson, K.K. de Mesy-Bentley, R. Waugh, and J. Palis. 2007. The megakaryocyte lineage

- originates from hemangioblast precursors and is an integral component both of primitive and of definitive hematopoiesis. *Blood*. 109:1433–1441. <https://doi.org/10.1182/blood-2006-06-031898>
- Trakala, M., S. Rodríguez-Acebes, M. Maroto, C.E. Symonds, D. Santamaría, S. Ortega, M. Barbacid, J. Méndez, and M. Malumbres. 2015. Functional reprogramming of polyploidization in megakaryocytes. *Dev. Cell*. 32: 155–167. <https://doi.org/10.1016/j.devcel.2014.12.015>
- Wright, J.H.. 1906. The origin and nature of blood platelets. *Boston Med. Surg. J.* 154:643–645. <https://doi.org/10.1056/NEJM190606071542301>
- Wright, J.H.. 1910. The histogenesis of the blood platelets. *J. Morphol.* 21: 263–278. <https://doi.org/10.1002/jmor.1050210204>
- Wu, D., and G.K. Smyth. 2012. Camera: a competitive gene set test accounting for inter-gene correlation. *Nucleic Acids Res.* 40. e133. <https://doi.org/10.1093/nar/gks461>
- Wu, D., E. Lim, F. Vaillant, M.L. Asselin-Labat, J.E. Visvader, and G.K. Smyth. 2010. ROAST: rotation gene set tests for complex microarray experiments. *Bioinformatics*. 26:2176–2182. <https://doi.org/10.1093/bioinformatics/btq401>
- Yamada, E.. 1957. The fine structure of the megakaryocyte in the mouse spleen. *Acta Anat. (Basel)*. 29:267–290. <https://doi.org/10.1159/000141169>
- Zhang, L., M. Orban, M. Lorenz, V. Barocke, D. Braun, N. Urtz, C. Schulz, M.L. von Brühl, A. Tirniceriu, F. Gaertner, et al. 2012. A novel role of sphingosine 1-phosphate receptor S1pr1 in mouse thrombopoiesis. *J. Exp. Med.* 209:2165–2181. <https://doi.org/10.1084/jem.20121090>
- Zheng, G.X., J.M. Terry, P. Belgrader, P. Ryvkin, Z.W. Bent, R. Wilson, S.B. Ziraldo, T.D. Wheeler, G.P. McDermott, J. Zhu, et al. 2017. Massively parallel digital transcriptional profiling of single cells. *Nat. Commun.* 8: 14049. <https://doi.org/10.1038/ncomms14049>
- Zucker-Franklin, D., and S. Petrusson. 1984. Thrombocytopoiesis--analysis by membrane tracer and freeze-fracture studies on fresh human and cultured mouse megakaryocytes. *J. Cell Biol.* 99:390–402. <https://doi.org/10.1083/jcb.99.2.390>

Supplemental material

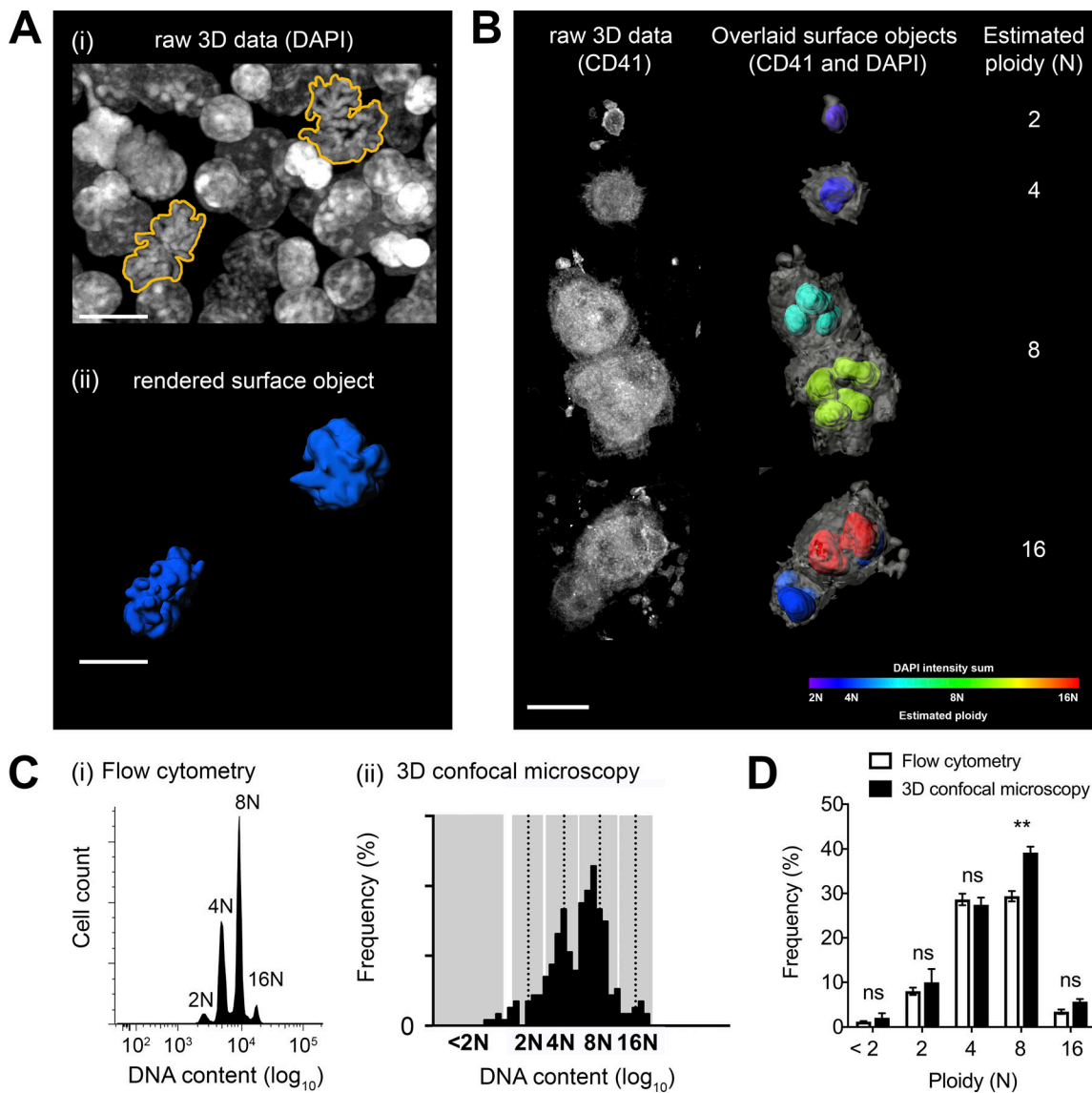


Figure S1. **Validation of in situ ploidy quantification in the E13.5 FL from high-volume 3D imaging data.** (A) Representative examples of non-Mk (CD41⁻) mitotic figures identified using DAPI staining (i) and the derived surface objects (blue) used as 4N references to normalize the DNA content of Mks in situ (ii). Scale bars, 5 μ m. (B) Nuclei within Mk surface objects (gray) pseudocolored (spectrum) according to DAPI intensity sum. Scale bar, 30 μ m. (C) Mk ploidy profiles derived from the gold-standard flow cytometry assay (i) and from 3D images (ii). (D) Other than a greater frequency of 8N Mks classified using the imaging method, the two ploidy analysis techniques were highly comparable ($n = 3$ independent experiments). $P = 0.008$, one-way ANOVA.

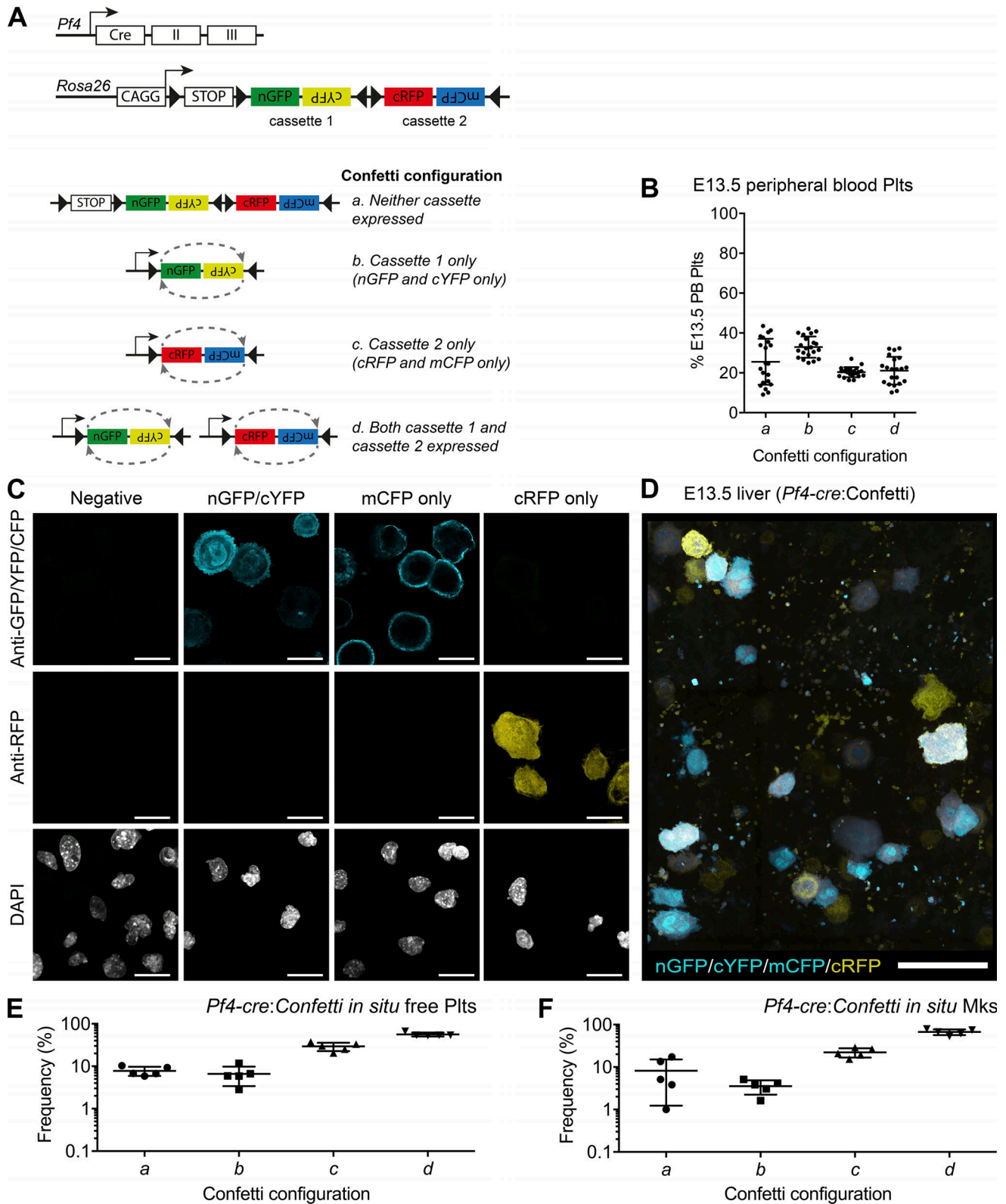


Figure S2. **Using the *Pf4-Cre:Confetti* system to determine the origin of Mk membrane buds.** (A) Schematic representation of the *Pf4-Cre:Confetti* system used to label Mks for identification of *Confetti* configurations *a-d*. (B) Quantification of *Confetti* configurations of E13.5 circulating Plts by flow cytometry ($n = 20$ mice). (C) MEFs derived from *R26R-Confetti* embryos were treated with recombinant TAT-Cre protein and purified by flow cytometry according to fluorescent protein expression. Anti-GFP antibody effectively detected nGFP, cYFP, and mCFP, and anti-RFP detected cRFP ($n = 2$ independent experiments). Scale bar, 30 μm . (D) With the exception of CFP, these antibodies effectively identified *Pf4-Cre:Confetti* configurations for Mks in high-volume 3D imaging of E13.5 FL: cassette 1 expression shown in blue; cassette 2 expression in yellow; coexpression of both cassettes 1 and 2 appear gray. Scale bar, 70 μm . (E and F) *Confetti* configuration scores of free Plts (E) and Mks (F) imaged in situ ($n = 5$ mice).

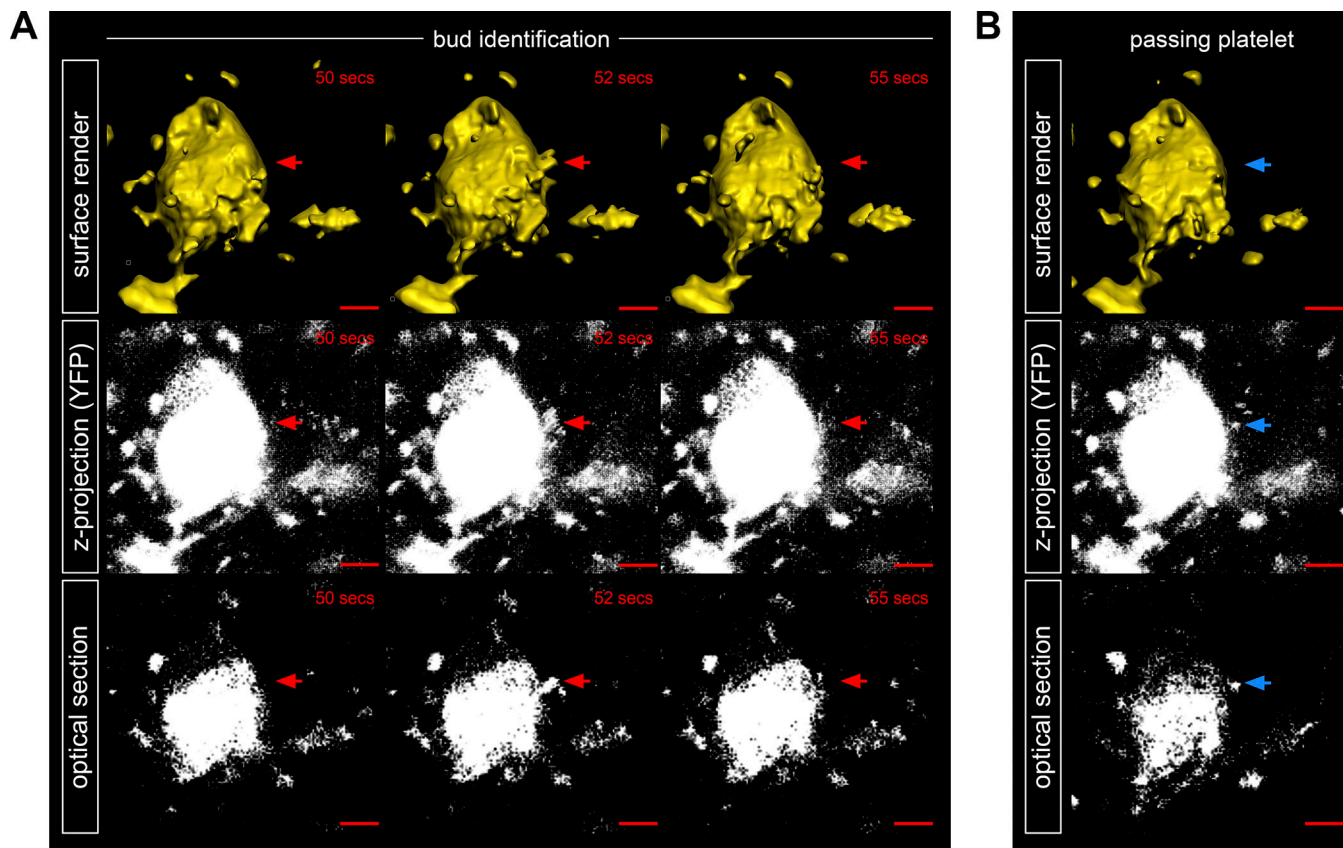


Figure S3. **Criteria used for membrane bud identification in *Pf4-Cre:YFP* ABM.** Plasma membrane buds were identified in high-time-resolution movies using a two-step process: (1) changes to the Mk membrane were initially identified using a surface rendering of YFP and confirmed using z-projection of the raw data; and (2) inspection of each optical section through the entire z-series. **(A and B)** Plt-like structures at the Mk membrane were classified as buds if they were continuous with the Mk (A); they were classified as passing Plts if no continuity was observed (B). Scale bars, 10 μ m. Red arrows in A indicate position of bud; blue arrows in B indicate the position of a passing Plt.

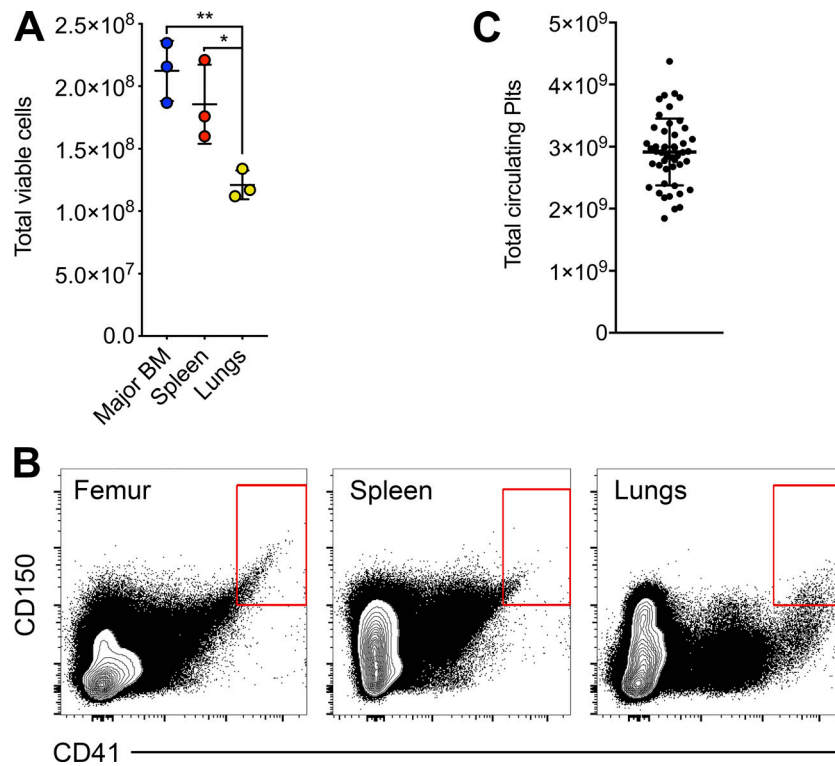


Figure S4. **Cellularity and Mk abundance in major Mk-containing organs.** (A) Total cellularity of all major BM-containing bones, spleen and lungs ($n = 3$ mice). **, $P = 0.008$; *, $P = 0.04$, one-way ANOVA with Tukey's multiple comparisons test. (B) Representative examples of the gating strategy used to identify mature Mks by flow cytometry in cell suspensions of femoral BM, spleen and lungs. Plots were derived from the exclusion of dead cells (7AAD⁺) and RBCs (TER119⁺); $n = 3$ mice. (C) Total number of circulating Plts in adult C57BL/6 mice ($n = 48$).

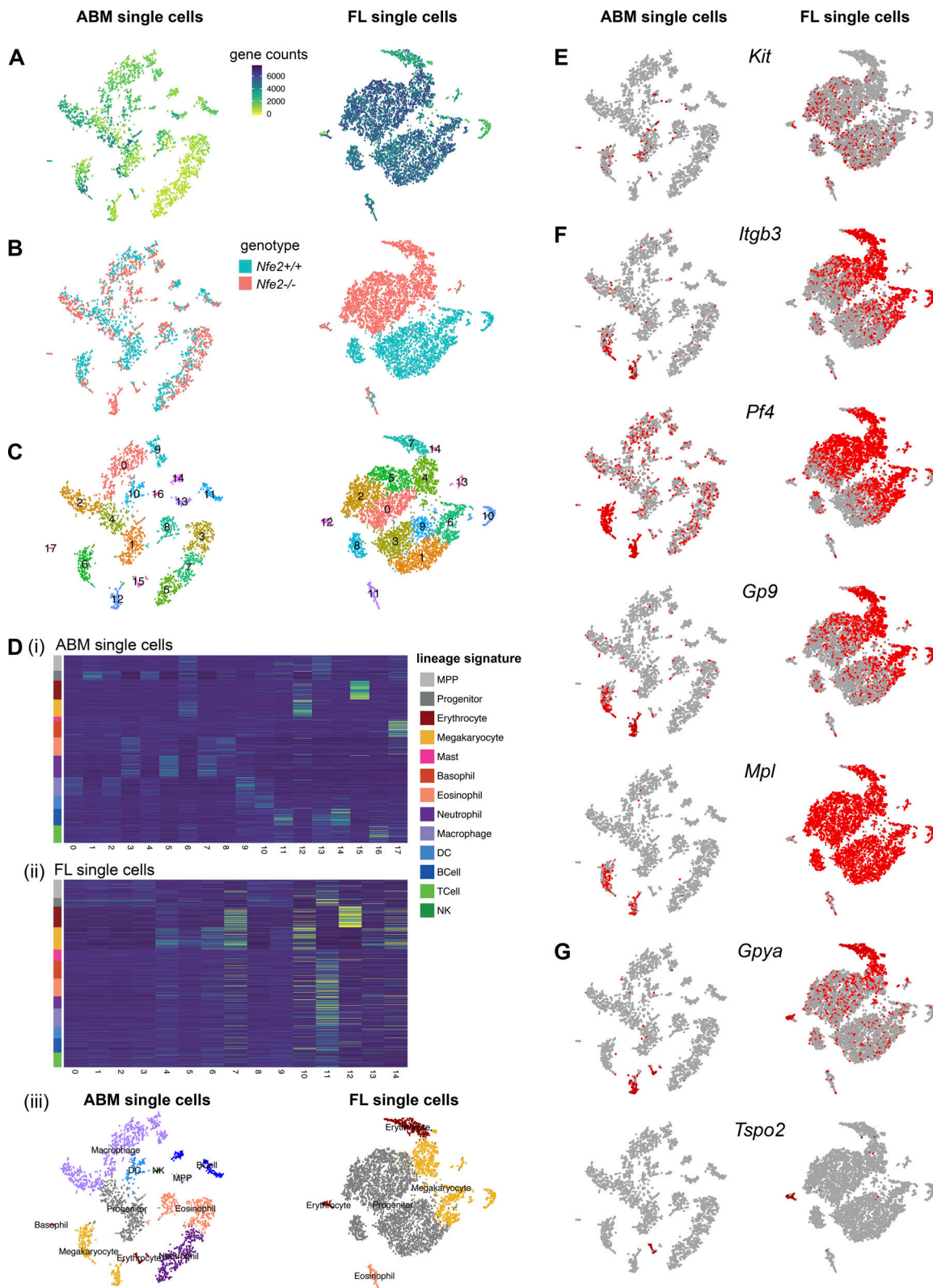


Figure S5. **Single-cell RNA-seq quality control metrics and lineage assignment.** (A–C) t-SNE (distributed stochastic neighbor embedding) plots from ABM and E13.5 FL samples overlaid with number of genes detected per cell (A); genotype of each cell (B); and unsupervised graph-based clustering (C). (D) Heatmap of the average expression of Haemopedia lineage signature genes in each cluster defined for ABM (i) or E13.5 (ii) samples. Only genes that were detected in the samples are shown. Cluster numbers as in C. Lineages assigned to each cluster using lineage signatures defined from Haemopedia mouse RNA-seq (iii). (E–G) Expression of lineage specific genes for each individual cell across tSNE plot: *Kit* (progenitor cell associated gene; E); *Itgb3*, *Pf4*, *Gp9*, and *Mpl* (Mk-associated genes; F); and *Gpya*, an erythroid associated gene whose expression was enriched in $Nfe2^{-/-}$ Mk cluster, and *Tspo2*, which is also an erythroid associated gene but was not detected in the Mk clusters (G).

Video 1. **Conversion of high-volume 3D images into quantifiable datasets.** Representative example of the use of surface objects to identify and quantify multiple parameters from free Plts and Mks in situ in E13.5 FL. Based on CD41 expression (gray signal from raw data), surface objects representing free Plts and Mks were generated; by filtering on object volume, free Plts (yellow) and Mks (gray) were distinguished. For Mks that passed quality control (complete volumes acquired), surface objects of nuclei were manually defined from sequential optical sections and rendered, from which DNA content/ploidy was estimated.

Video 2. **Ex vivo proPlt formation is rare but can occur from Mks during E13.5 FL organotypic culture.** Video depicts a proPlt forming Mk (gray) that undergoes the classic changes in volume and sphericity typical of the process. Initiation of proPlt formation is represented by the formation of a leading edge. Time shown as hours:minutes:seconds. Original data = 1 frame (z-stack) every 3 min.

Video 3. **Direct release of membrane buds occurs within the E13.5 FL environment without engaging proPlt formation.** Representative video depicting the formation and release of Mk membrane buds in E13.5 FL cultures, giving rise to nascent Plts. Both raw data (CD41, left) and rendered surface objects (right) are shown. Mk and nascent Plts released from the same Mk colored yellow. Colored arrows are used to distinguish individual buds. Time shown as hours:minutes:seconds. Original data = 1 frame (z-stack) every 2.5 min.

Video 4. **FL Mks bud directly into the peripheral circulation.** Video of E13.5 FL Mk from Fig. 4 E showing the delivery a Plt-sized VWF-loaded membrane bud into the lumen of a blood vessel. The video begins showing a z-projection of a CD41-expressing Mk (gray) in close association with the *Flk1*-GFP-expressing vasculature (green), then transitions to show surface object rendering of both the Mk and vasculature, then to an optical section through the z-projection revealing the presence of VWF (red) in the bud.

Video 5. **Large-scale 4D whole calvarial BM imaging.** Representative video illustrating real-time interaction with 4D whole BM intravital time course data from *Pf4-Cre:mTmG* reporter mice using Fiji software. This video illustrates the ability to visualize a large number of Mks by moving in the x, y, and z axes of data more than ~6 h of imaging in live adult mice. By taking this approach, the behavior of all Mks in the calvarial BM can be observed and quantified, allowing detailed analysis of individual Mks and the organ as a whole system. The cursor highlights movement within the individual dimensions of the dataset and an example of proPlt production by a single Mk. This video is representative of three individual biological replicate datasets. Data presented here has been downsampled in resolution for uploading purposes. Green, Mks/Plts; gray, bone (SHG); red, non-Mk cells/stroma. Original data = 1 frame (z-stack) every 3.5 min.

Video 6. **ProPlt formation in the BM is a slow process.** Representative video showing the slow process of proPlt formation. Mks are labeled by *Pf4-Cre:YFP* (gray). Time shown as hours:minutes:seconds. Original data = 1 frame (z-stack) every 3.5 min.

Video 7. **Thick extensions from Mks with complex morphology do not produce proPlts.** Video shows Mks (*Pf4-cre:YFP*, gray) which, despite displaying complex morphologies, do not generate proPlts. Video represents continuous imaging at 3.5-min time resolution for ~4 h. Time shown as hours:minutes:seconds. Original data = 1 frame (z-stack) every 3.5 min.

Video 8. **Mk membrane budding in the ABM.** 4D (3D z-projection + time) videos of three representative examples of Mks releasing Plts directly into the peripheral blood. In contrast to proPlt formation, this is an exceptionally rapid process. Mks are labeled by *Pf4-Cre:YFP* (gray). Arrows indicate the location of membrane buds (all of which were confirmed by inspection of individual z-positions). Time shown as hours:minutes:seconds. Original data = 1 frame (z-stack) every 2–3 s.

Video 9. **Mk exit from the BM space after proPlt formation.** 3D video of an example of an Mk exiting the BM space during the process of proPlt formation. Data were acquired at single z-positions at 15 frames/s. For the purposes of presentation, data has been reduced in temporal resolution 20-fold and rendered at 100 frames/s. Mks labeled by *Pf4-Cre:mTmG* (Tomato is red and GFP is green). Time shown in seconds.

Tables S1–S8 are provided online in Word files. Table S1 lists antibodies and protein detection reagents used. Table S2 shows metrics associated with generation of Mk scRNA-seq data. Table S3 lists commonly down-regulated genes in *Nfe2^{-/-}* Mks versus *Nfe2^{+/+}* Mks. Table S4 lists commonly up-regulated genes in *Nfe2^{-/-}* Mks versus *Nfe2^{+/+}* Mks. Table S5 is a complete list of GO biological process terms enriched from commonly down-regulated genes in *Nfe2^{-/-}* Mks versus *Nfe2^{+/+}* Mks. Table S6 summarizes the base values used to estimate Plt production (as outlined in Materials and methods). Table S7 lists the parameters used to estimate potential Plt yield from BM and lung Mks. Table S8 compares Plt production via proPlt formation and membrane budding. Data S1 and S2 list the different genes used.